



# Constraints on the Lithospheric Structure and Rheology of Northern Chile from 8-year Post-Seismic Deformation following the $M_w$ 8.1 Iquique Earthquake

Juliette Cresseaux<sup>1</sup>, Mathilde Radiguet<sup>1</sup>, Marie Pierre Doin<sup>1</sup>, Marcos Moreno<sup>2</sup>, Flora Huiban<sup>1,6</sup>, Mathilde Marchandon<sup>3</sup>, Juan Carlos Baez<sup>4</sup>, Aubin Tsapong Tsague<sup>1</sup>, Gaël Janex<sup>1</sup>, Andres Tassara<sup>5</sup>, and Anne Socquet<sup>1</sup>

<sup>1</sup>University Grenoble Alpes, University Savoie Mont Blanc, CNRS, IRD, University Gustave Eiffel, ISTERre, 38000 Grenoble, France

<sup>2</sup>Departamento de Ingeniería Estructural y Geotécnica, Pontificia Universidad Católica, Santiago, Chile

<sup>3</sup>Department of Earth and Environmental Sciences, LMU Munich, Germany

<sup>4</sup>Centro Sismológico Nacional, Santiago, Chile

<sup>5</sup>Departamento de Ciencias de la Tierra, Facultad de Ciencias Químicas, Universidad de Concepción, Concepción, Chile

<sup>6</sup>Current address, Department of Geosciences and Natural Resources Management, University of Copenhagen, 1350, Copenhagen, Denmark

**Correspondence:** Anne Socquet (anne.socquet@univ-grenoble-alpes.fr)

## Abstract.

Understanding and modeling the deformation following large earthquake is essential for characterizing the rheological structure and processes that release post-seismic stress. Here, we measured postseismic deformation over an 8-year period following the 2014  $M_w$  8.1 Iquique earthquake using Sentinel-1 InSAR and GNSS time series in northern Chile and Bolivia. We jointly modeled the surface displacements caused by afterslip and viscoelastic relaxation using a two-dimensional finite element model. The combination of GNSS and InSAR data allows us to continuously map the temporal and spatial variations of the displacement field, especially in the vertical component, providing valuable constraints for modeling the rheological structure of the continental plate from the slab to the Altiplano. The amplitude of the uplift pattern claims for a weak zone below the western part of the Altiplano, where the volcanic arc is fed by partial melting. To reproduce the temporal evolution of post-seismic uplift, this weak zone must be governed by a Burgers rheology, combining a transient Kelvin body with a viscosity  $\eta_{Kwz} = 2 \times 10^{18} Pa.s$  and a Maxwell body with a viscosity  $\eta_{Mwz} = 2 \times 10^{19} Pa.s$ . To the west, our preferred model includes a cold nose rooting into the slab at a slab-mantle decoupling depth of  $d_{CN} = 84$  km. This near-trench elastic wedge, predicted by thermal models, drives mantle flow and generates surface uplift during post-seismic relaxation. By characterizing the post-seismic deformation field following the Iquique earthquake, our results refine the rheological structure below the Central Andes and define its response to stress changes down to short time scales.



## 1 Introduction

The aftermath of large earthquakes often entails prolonged visco-elastic relaxation, resulting in regional-scale deformation that can persist for several decades (Wang, 2007; Hu et al., 2004; Suito and Freymueller, 2009; Wang et al., 2012). Exploration of post-seismic deformation following megathrust earthquakes has proven pivotal in refining our understanding of mantle viscosity for both oceanic and continental regions (e.g., [Pollitz2006post, Panet2010upper, Suito2017importance, Li2017PostseismicRheology, Boulze2022post]. Many previous studies have shown that using transient viscosity rheology more effectively captures the time evolution of post-earthquake deformation (Sun et al., 2014; Hu et al., 2016; Klein et al., 2016). Furthermore, the analysis of post-seismic deformation offers valuable insights into the rheological structure of the overriding plate (Pollitz et al., 2008; Li et al., 2018; Muto et al., 2019, e.g.). For example, Luo and Wang (2021a) demonstrated that the rigid cold forearc mantle (commonly known as the cold nose), shaped by the thermal structure of subduction zones (Wada et al., 2008; Wada and Wang, 2009), significantly influences modeled vertical surface displacements resulting from post-seismic mantle corner flow. Other studies have shown that a weak zone within the overriding plate modifies the post-seismic response by localizing the deformation in this area (Rousset et al., 2012; Itoh et al., 2021).

In the Central Andes, large-scale structural features are well-constrained by geophysical studies, revealing that the rigid Brazilian lithosphere, approximately 130 km thick, substantially thinned to 70–80 km beneath the Altiplano. This region also has a thick crust (60–70 km) characterized by a thin elastic layer ( $\sim 20$  km) atop a weak lower crust (Tassara et al., 2006; Tassara and Echaurren, 2012; Giambiagi et al., 2022). The weakened zone is consistent with predictions from numerical simulations of small-scale flow within the hydrated subduction mantle wedge, which suggest reduced rock strength and thermal erosion in the upper plate (Arcay et al., 2005; Babeyko et al., 2002; Sobolev and Babeyko, 2005; Pons et al., 2022; Wang et al., 2021). Despite these insights, the precise extent and rheology of this weak zone remain poorly characterized. Fundamental questions persist: How wide is the weak zone? How does it relate to the topography? How low is its viscosity? Does its rheology evolve with time during the post-seismic relaxation? How does it affect the deformation during the seismic cycle?

The post-seismic deformation following the 2014 Iquique earthquake offers an excellent opportunity to explore the rheological structure of the overriding continental plate. Existing studies on post-seismic deformation after the Iquique earthquake have primarily focused on the afterslip process (Shrivastava et al., 2019; Itoh et al., 2023). Only two studies (Hu et al., 2021; Hoffmann et al., 2018) have addressed the influence of visco-elasticity on the surface displacement field, but these are limited by the short observation period (2 or 4 years) and show a suboptimal fit, particularly with respect to vertical displacements. In this study, we take advantage of the monitoring of the deformation by permanently installed GPS stations in northern Chile and Bolivia, and combine it with Sentinel-1 InSAR time series to delineate the spatial pattern of the post-seismic deformation and its temporal evolution over an 8-year period following the earthquake. InSAR shows a strongly deformed area, extending from the forearc to the arc, that is resulting from viscoelastic relaxation in the weak zone. We model the surface displacement generated by afterslip and visco-elastic relaxation following the co-seismic rupture using a Finite Element Model in two dimensions. Our objective is to perform a parametric exploration of the geometry in order to constrain the geometry of the cold nose and of the weak zone, and to explore its rheology. The use of a simple 2D model, rather than a 3D model, allows us to



50 test various configurations against the data. The spatial continuity of the deformation field provides excellent constraints on the localization of the deformation, enabling us to refine our understanding of the rheological structure of the continental plate from the subduction zone to the Altiplano.

## 2 Seismotectonic Setting of the 2014 Iquique Earthquake

Stretching over 8000 km, the Peru-Chile trench delineates the boundary between the Nazca and South American plates and has played a crucial role in the formation and seismic activity of the Andes Cordillera. This subduction zone is segmented along strike and ruptures into large earthquakes (Métois et al., 2016; Molina et al., 2021). The 1960  $M_w$ 9.5 Valdivia earthquake was the largest earthquake instrumentally recorded worldwide (Kanamori, 1977). It ruptured a 920 km-long section of the subduction zone (Cifuentes, 1989), and was followed by prolonged visco-elastic relaxation and seismic quiescence that lasted for several decades (Hu et al., 2004; Moreno et al., 2011; Ruiz et al., 2017).

60 More recently, three mega-earthquakes ruptured the Chilean subduction zone: Maule, 2010,  $M_w$ 8.8 (Moreno et al., 2010; Lin et al., 2013); Iquique, 2014  $M_w$ 8.1 (Ruiz et al., 2014; Schurr et al., 2014; Duputel et al., 2015) and Illapel, 2015  $M_w$ 8.3 (Tilmann et al., 2016; Heidarzadeh et al., 2016). The post-seismic visco-elastic relaxation that followed the 2010  $M_w$ 8.8 Maule earthquake has been investigated in various studies. Klein et al. (2016) suggest that a weak mantle (with a viscosity of  $4.75 \cdot 10^{18}$  Pa.s) and a viscous channel along the slab interface to model the afterslip are required to explain the GNSS observations. To model the uplift observed 300 km from the trench, Li et al. (2017) incorporated a mantle with a low viscosity beneath the Main Cordillera that increases toward the Argentinian craton. At 700 km from the trench, a remarkably high viscosity of  $10^{30}$  Pa.s is required to account for the observed subsidence in the far-field, which, over the time scale considered, is equivalent to an elastic behaviour. Additionally, Li et al. (2018) emphasized that viscosity increases not only with the distance from the trench but also with time after the earthquake. Studies focusing on the aftermath of the 2015  $M_w$ 8.3 Illapel earthquake have predominantly delved into afterslip and aftershock seismicity (Poli et al., 2017; Twardzik et al., 2021; Shrivastava et al., 2016; Tissandier et al., 2023; Hormazábal et al., 2023). Nevertheless, a comparative analysis of post-seismic visco-elastic relaxation following the three most recent megathrust earthquakes in Chile pleads for a linear, Newtonian, viscosity in the asthenosphere (Boulze et al., 2022). Additionally, the continuous geodetic monitoring over the years since these earthquakes offers data to evaluate the rheological impact on the observed post-seismic deformation.

75 The  $M_w$ 8.1 Iquique earthquake occurred on the 1<sup>st</sup> of April 2014, with its epicenter located  $-70.79^\circ$  East and  $-19.62^\circ$  North (see Figure 1). It ruptured the central part of a mature seismic gap that had last been ruptured in 1877 by a  $M_w$ 8.6+ event (Comte and Pardo, 1991; Métois et al., 2013; Béjar-Pizarro et al., 2013; Vigny and Klein, 2022). However, smaller magnitude earthquakes have also struck the gap, such as the 2005  $M_w$ 7.8 Tarapacá intraslab intermediate-depth earthquake (Peyrat et al., 2006; Jara et al., 2017) and the 2007  $M_w$ 7.7 Tocopilla deep subduction earthquake (Béjar-Pizarro et al., 2010). This earthquake was also preceded by a slow slip event and a foreshock sequence (Socquet et al., 2017; Ruiz et al., 2014; Schurr et al., 2014).

The Iquique earthquake ruptured the subduction interface between depths of 15 and 55 km over a  $\sim 50$  km wide area, with a peak slip of 9 meters (Duputel et al., 2015; Jara et al., 2018). Following the mainshock, a significant aftershock of magnitude

7.7 occurred about 120 km further south (Duputel et al., 2015; Jara et al., 2018) (Figure 1). Itoh et al. (2023) focused on the early afterslip occurring during the 27 hours separating the mainshock from its largest aftershock using high-rate GNSS data. Given the notably high magnitude of this aftershock compared to the mainshock, its contribution should be considered in any post-seismic relaxation model. Subsequent post-seismic deformation was investigated using GNSS time series until the end of 2014 (Shrivastava et al., 2019), and during the first two years, reaching a maximum of  $\sim 89$  cm of afterslip on the slab interface at depths of 40-50 km (Hoffmann et al., 2018). However, a two-year time-frame is insufficient to distinguish between afterslip and visco-elastic relaxation. Hu et al. (2021) modeled viscoelastic relaxation and proposed the presence of a 110 km thick low-viscosity layer ( $2.10^{18}$  Pa.s) beneath the slab, along with oceanic and continental mantle viscosities of  $1.10^{20}$  and  $3.10^{19}$  Pa.s, respectively. They also included a weak shear zone to model afterslip. However, this study is limited by the availability of GNSS time series and shows a suboptimal fit, especially for vertical displacements. Therefore, the temporal evolution of deformation after the Iquique earthquake and the role of the rheological structure in viscoelastic relaxation remain poorly understood.

## 3 Data

### 3.1 InSAR velocity maps

The arid climate in South Peru and North Chile makes it the ideal area to process interferometric data. This region is covered by two Sentinel-1 tracks, ascending (A149) and descending (D054). We processed all available acquisitions from October 2014 to December 2019, thus covering a duration of slightly over 5 years, with 183 dates for track A149 and 145 dates for track D054. We used the small baseline subset method with the NSBAS processing chain that goes from raw data to time series analysis and includes image coregistration, spectral diversity correction, mitigation of atmospheric delays, filtering and unwrapping, as described in Doin et al. (2011). It is partly based on the ROIPAC software (Rosen et al., 2004) and adapted to Sentinel-1 data processing following Grandin (2017). More processing details can be found in Thollard et al. (2021). The network of interferograms is defined and calculated with temporal and perpendicular baseline constraints. Interferometric pairs were computed with  $n/n+1$  (an acquisition  $n$  with the following acquisitions  $(n+1)$ ), then the pairs  $n/n+2$ ,  $n/n+4$ , plus interferometric pairs with both a temporal baseline around 12 months and a perpendicular baseline smaller than 100 meters. This strategy results in 514 (710, respectively) interferograms for track A149 (D054, respectively). The contribution of the stratified atmosphere is corrected using the ERA-5 global atmospheric reanalysis produced by ECMWF (European Centre for Medium-Range Weather Forecast) (Doin et al., 2009; Jolivet et al., 2011). Unwrapped interferograms are flattened with linear ramps in range and azimuth, as explained in Thollard et al. (2021), that removes the effects of solid earth tides, of rigid plate movement in ITRF reference frame, and some ramps associated with the ionosphere (Lemrabet et al., 2023; Marconato et al., 2024). The interferometric network is then inverted into time series (López-Quiroz et al., 2009; Ho Tong Minh et al., 2022). The interferometric network misclosure is very low for the two time series, showing the absence of residual unwrapping errors and a low phase noise due to temporal decorrelation.

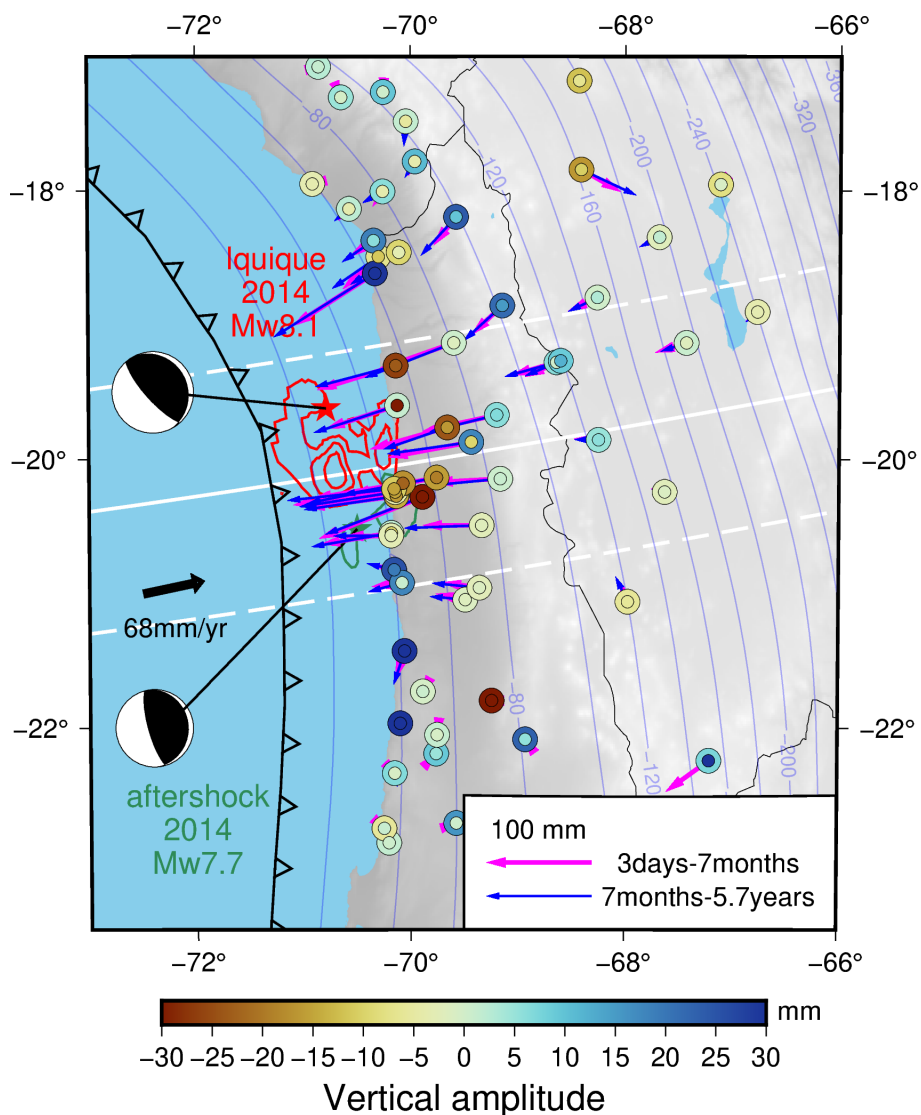


**Figure 1.** Seismo-tectonic context of the Iquique earthquake. The red and green stars display the locations of the epicenter of the Iquique earthquake and that of the major aftershock of magnitude 7.7, respectively, whereas the red and green contours represent their respective co-seismic slips from Jara et al. (2018). The circles represent the location of the GNSS stations. The white line and dotted lines show the studied cross-section  $\pm 100$  km. The black bold arrow shows the convergence direction of the subduction. The blue lines describe the slab isodepth contours. The color of the inner (outer, respectively) circles represent the vertical displacements of the GNSS stations during the period between 2 days to 7 months (7 months to 5.7 years, respectively) after the earthquake. The purple (blue, respectively) arrows represent the horizontal displacements of the GNSS stations during the period between 2 days to 7 months (7 months to 5.7 years, respectively) after the earthquake.



115 The phase delay time-series is affected by large residual tropospheric delays, especially during the austral summer and, to a lesser extent, by ionospheric phase screens. To extract the ground displacement, the InSAR time series is fitted using a simple trajectory model consisting of a linear term representing the interseismic loading, a logarithm decay representing post-seismic relaxation, and a seasonal term, using the equation:

$$\Phi(t) = \underbrace{v \times t}_{\text{interseismic loading}} + \underbrace{A \times \log(1 + (t - t_{Iq})/\tau)}_{\text{post-seismic relaxation}} + \underbrace{B \times \cos(2\pi t) + C \times \sin(2\pi t)}_{\text{seasonal term}} \quad (1)$$

120 where  $v$ ,  $A$ ,  $B$  and  $C$  are parameters,  $t$  is the acquisition time,  $t_{Iq}$  is the Iquique earthquake time and  $\tau$  is the relaxation time. Each time step in equation 1 is inversely weighted by the atmospheric phase screen amplitude to decrease the influence of summer acquisitions and of outliers, as detailed in Lemrabet et al. (2023). We found that we cannot constrain the relaxation time with InSAR data, as the time series starts seven months after the earthquake, moreover during a noisy summer season. Therefore, we fixed  $\tau$  to 45 days.

125 The estimations of  $v$  and  $A$  are anticorrelated as the variables  $t$  and  $\log(1 + (t - t_{Iq})/\tau)$  are positively correlated over the time series duration. Because of this, and because of the large tropospheric noise during the summer seasons, we keep both, the interseismic loading and the post-seismic relaxation to correct from the seasonal variations. Then we extract from InSAR the cumulated displacement,  $d_{cumul}$ , using:

$$d_{cumul} = v \times (t_{end} - t_{start}) + A \times \log(1 + (t_{end} - t_{Iq})/\tau) - A \times \log(1 + (t_{start} - t_{Iq})/\tau)$$

We correct the cumulated displacement from the interseismic loading effect using the predictions of coupling model of  
130 Jolivet et al. (2020), projected into the Line Of Sight (LOS) and obtain LOS cumulated displacement maps of the post-seismic deformation. For track D054, we miss far-field InSAR information, where we could assume a zeroing post-seismic signal (Figure 2). We choose to reference the cumulated post-seismic InSAR maps using GNSS data available within the tracks. As will be shown in section 3.2, we computed the east, north and up components of the post-seismic GNSS time series between  $t_{start}$  and  $t_{end}$ , and project them in LOS (Figure 2). The differences between GNSS and InSAR cumulated post-seismic  
135 displacements is fitted by a linear function of range and azimuth, that is then added to InSAR post-seismic maps.

The obtained cumulative displacement maps of the ascending and descending tracks are presented in Figure 2. On the ascending track (A149) on the left, a deformation pattern towards the LOS is clearly seen affecting the entire width of Chile. On the descending track (D054) on the right, a pattern away from the LOS is seen, it has less amplitude and the general pattern is less clear than the track A149. To obtain the trench perpendicular evolution of the cumulative displacement, the displacement  
140 is extracted along a section by computing the mean value every 10 km, over 125 km on each side of the section.

### 3.2 GNSS

The GNSS time series used in this study consist of 25 stations from different networks located in Chile (CSN, IPOC) and Bolivia (UNAVCO) (Foster et al., 2014). Data processing is similar to Lovery et al. (2024) and position time series are available

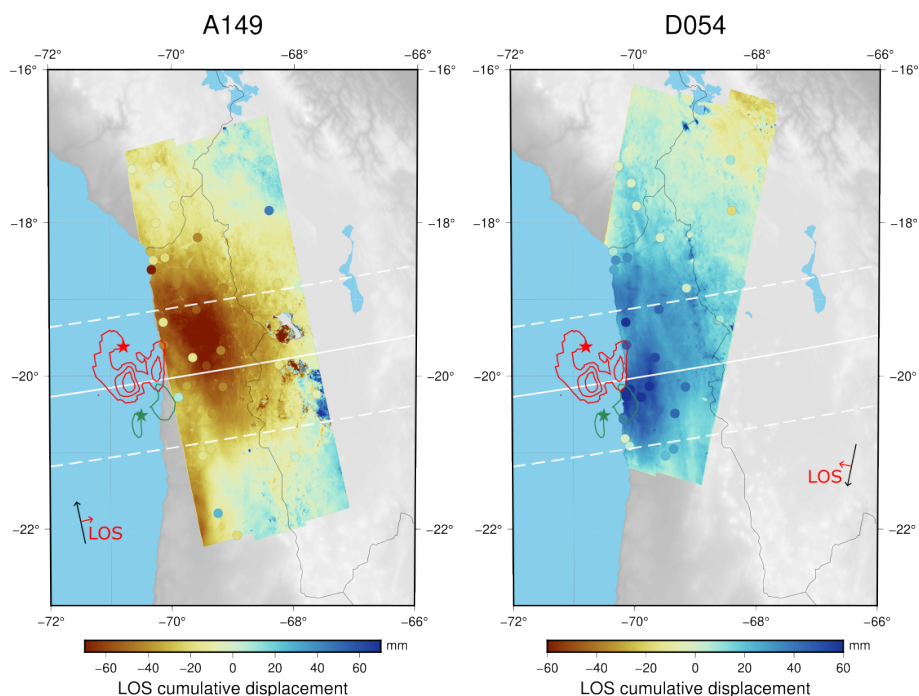


**Figure 2.** Maps of the InSAR cumulative displacements between October 2014 and December 2019, corrected from interseismic displacement and referenced using GNSS data. Colored dots show the GNSS cumulative displacements during the InSAR-period, projected in the LOS. Left: ascending track A149. Right: descending track D054. The red star shows the location of the epicenter of the Iquique earthquake and the red lines the associated slip contours from Jara et al. (2018). The green star denotes the epicenter of the aftershock. The solid white line shows the location of the section and the dotted white lines the section  $\pm 100$  km.

through Socquet et al. (2023). The location of the stations is presented in Figure 1 and a map with the associated names can be found in the Figure A1. Rinex data were processed using the GipsyX software version 1.5 from the Jet Propulsion Laboratory (JPL) (Bertiger et al., 2020). The phase ambiguity was resolved using wide-lane phase bias constraints provided by JPL. JPL's final orbit and clock products and NNR orbits are used. Bi-frequency observables are used to cancel ionospheric delays. The vertical tropospheric zenith delays are inverted every 5 minutes and two horizontal gradients are accounted for per session of 24 hours, using VMF1 (Boehm et al., 2006). Multi-path and phase center stability corrections are obtained with antenna calibration tables and by averaging the GNSS positions to keep one position per 24h. The FES 2014b model is used to correct from ocean tide loading (Lyard et al., 2021). We then apply a Helmert transform to map the loose NNR solution in the IGS2014 (Altamimi et al., 2016), using the scaling, rotation and translation factors provided by JPL.

We analyze the time series between 2010 and 2022. Beginning in 2010 allows us to avoid the important contribution of the post-seismic signal that followed the  $M_w 7.7$  2007 Tocopilla and the  $M_w 8$  1995 Antofagasta earthquakes. We are mostly interested in the 8 years of post-seismic data following the Iquique earthquake in 2014, which allows us to study the post-seismic deformation process over a long time scale. For eight stations listed in Appendix A, the time series does not have



160 sufficient data before the Iquique earthquake to make a robust estimate of a linear interseismic trend. In that case, we use the interseismic trends predicted by the interseismic model from Jolivet et al. (2020). To be in the same reference frame as the interseismic model from Jolivet et al. (2020), we rotated the time series in the South America stable reference (SOAM) using the rotation between NNR-Nuvel-1A to SOAM (-25.4°N, -124.6°E, 0.11°/yr) and then account for a sliver modeled as a translation with a velocity of 5.4mm/yr to the North and 10.2mm/yr to the East (Jolivet et al., 2020).

165 To isolate the contribution of the post-seismic signal of interest in the GNSS time-series, and correct from other sources of deformation (interseismic, co-seismic, antenna jumps, seasonal variations), we use a trajectory model inspired by Bevis and Brown (2014) and developed by Marill et al. (2021). The position time series  $x(t)$  is modeled, for each station, with the following relation:

$$\begin{aligned}
 x(t) = & x_R + \underbrace{v(t - t_R)}_{\text{interseismic}} + \underbrace{\sum_{k=1}^2 [s_k \sin(2k\pi(t - t_R)) + c_k \cos(2k\pi(t - t_R))]}_{\text{seasonal variations}} \\
 & + \underbrace{\sum_{a=1}^{n_A} b_a H(t - t_a)}_{\text{antenna changes}} + \underbrace{\sum_{j=1}^{n_J} c_J H(t - t_J)}_{\text{co-seismic}} + \underbrace{m_{Iq} H(t - t_{Iq}) \times \log_{10}\left(1 + \frac{t - t_{Iq}}{\tau}\right)}_{\text{post-seismic}}
 \end{aligned} \quad (2)$$

170 with  $x_R$  the initial position,  $t_R$  the reference time,  $s_k$  and  $c_k$  seasonal variations amplitudes,  $n_A$  the number of antenna jumps and  $t_a$  the time of the antenna jumps,  $b_a$  the amplitude of the antenna jumps,  $n_J$  the number of co-seismic jumps,  $t_J$  the time of the co-seismic jumps,  $c_J$  the amplitude of the co-seismic jumps,  $t_{Iq}$  the Iquique earthquake time,  $\tau$  the relaxation time of the Iquique earthquake,  $m_{Iq}$  the amplitude of the post-seismic relaxation of the Iquique earthquake and  $H$  the Heaviside function. The influence radius of an earthquake has been adapted from the Nevada Geodetic Laboratory and is given by:  $r(M_W) = 10^{(0.5M_W - 0.8)/1.28} \text{ km}$  with  $M_W$ , the magnitude of the earthquake. The parameters are inverted using a multi-step iteration procedure (see Marill et al. (2021)). The fit of the trajectory model to the data is shown in the Figures A2 to A26 for each station. For the initial fit, we consider a constant value of  $\tau_R = 45$  days, which might not be optimal for all the time series  
 175 but does not significantly impact the estimates of other parameters. Mismodeled signals will be preserved in the residuals time series. Our post-processed time series consists of the original data corrected from a linear interseismic term, seasonal terms (annual and semi-annual), co-seismic offsets and antenna jumps, thus keeping only the displacements due to the post-seismic relaxation and noise.

180 We then further analyze the post-Iquique time series, starting on the 4<sup>th</sup> of April, one day after the April 3<sup>rd</sup>  $M_w 7.7$  aftershock, so that our results are not affected by the co-seismic displacements of this aftershock. We select 25 stations located around a profile of 100 km width, centered on the co-seismic patch (See Figure 1). The time series from those stations is further modeled to estimate the spatial variability in the amplitude ( $m_i$ ) and temporal evolution ( $\tau_i$ ) of the post-seismic signal between the near-field (close to the trench) and the far-field. To do so, we fit the GNSS time series with a logarithmic model and a variable time constant  $\tau_i$  for each station  $i$ , using the equation:



185 
$$x_i(t) = A_i + m_i * \log_{10}\left(1 + \frac{t - t_{Iq}}{\tau_i}\right) \quad (3)$$

where  $m_i$  is the amplitude,  $\tau_i$  is a time constant characterizing the relaxation and  $A_i$  is a constant corresponding to an offset if the pre or co-seismic is poorly inverted. The GNSS time series contains considerable data gaps, in particular missing data right after the earthquake for several stations, or missing data for the more recent time (see Figure 3). Our strategy to model the post-seismic signal using equation 3 will thus vary depending on the completeness of the time series.

190 When the time series has data just after the earthquake, we fix the constant  $A_i$  so that the model and data equal 0 for the first data point. In that case, we invert for the amplitude  $m_i$  and the time constant  $\tau_i$  for the East component time series, as it has the strongest signal amplitude. For the North and Vertical components, we only invert for the amplitude  $m_i$ , with  $\tau_i$  equal to the value inferred for the East component. A grid search between the amplitude and the relaxation time is then done to estimate the trade-off between the parameters, and obtain uncertainties for our time-series modeling (see Figure A27 for an example  
195 of the grid search and uncertainty estimation). The time series is resampled using a logarithmic sampling to give more weight to the short-term data with respect to long-term trends in the model fit. The Root Mean Square (RMS) is calculated with the following formula:  $RMS_i = \sqrt{(\sum_t^{n_t} (d_{obs}^{log}(t) - x_i^{log}(t))^2 / n_t)}$  where  $d_{obs}^{log}$  are the resampled data,  $x_i^{log}$  the logarithmic model and  $n_t$  the number of resampled data. The grid search gives the best combination of amplitude and relaxation time for the time series. The data and best model fit are plotted in Figure 3. The uncertainty associated with a modeled time series is computed  
200 using three times the RMS of the best model.

For the stations without data for several months after the earthquake or with a post-seismic signal of very low amplitude (SCRZ and URUS) (in grey on the Figure 3), we cannot constrain the relaxation time  $\tau_i$  so we fix  $\tau_i$  to the value inverted for the closest station with enough reliable data: for the stations in Bolivia, in far-field, we imposed the one of COLC and for HMBS, we imposed the relaxation time of CGTC. For these stations, we invert for the offset  $A_i$  in addition to the amplitude  $m_i$ . We also  
205 perform a grid search on the amplitude  $m$  and offset  $A$  to search for the best parameters and estimate uncertainties (see Figure A28). As for the stations with data just after the earthquake, the time series is resampled logarithmically. The best models for different stations are plotted in Figure 3. We consider as acceptable the parameter range for which  $RMS \leq 1.5 \times RMS_{best}$ ,  $RMS_{best}$  being the RMS of the best-fit model (see ellipse in Figure S27). We consider the highest and lowest amplitude models from this range of acceptable models to build a lower and upper bound on the displacements for each time series, and estimate  
210 the uncertainties on our time series.

In the following, the data are presented either as time series to investigate the temporal evolution (Figures 5 and 13) or spatially along a cross-section perpendicular to the trench (Figures 6 to 12, 14 and 15). In the cross sections, we plot the cumulative displacements for two different periods: the short-term period from 3 days to 7 months after the mainshock, and the long-term period from 7 months to 5.7 years after the mainshock. This second period corresponds to the acquisition period  
215 of InSAR data. For the GNSS time series, if data are present for a given station and a given date, we use a mean position over 10 days at that date. If the data are missing, we use the modeled time series (from equation 3) to extrapolate the position and

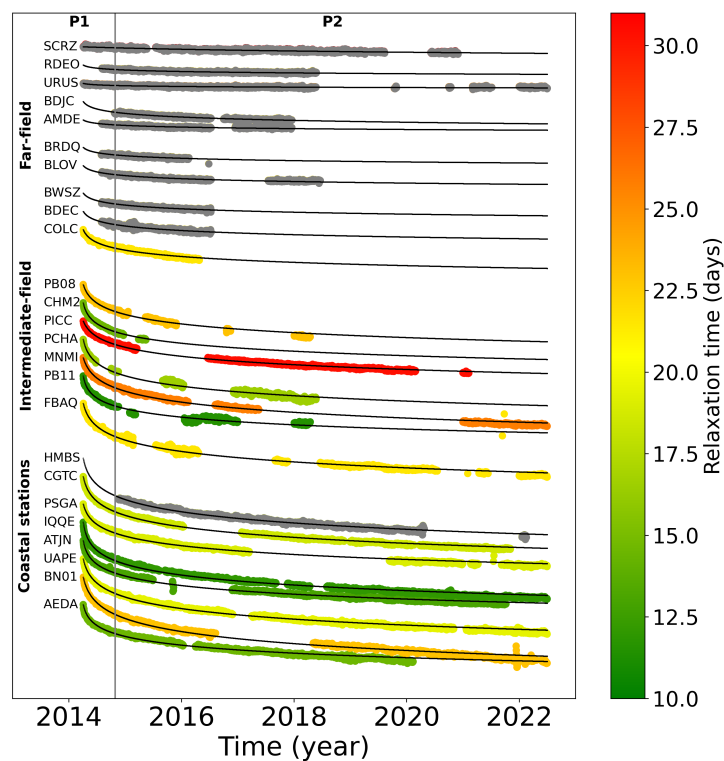


**Figure 3.** East components of time series depicting post-seismic displacements for the selected 25 stations ordered by distance to the trench. We can notice three subsets of stations as a function of the distance to the trench: the coastal stations from AEDA to HMBS ( $\leq 150$  km from the trench), the intermediate-field stations, from FBAQ to PB08 (between 150 and 250 km from the trench) and finally the far-field stations from COLC to SCRZ ( $\geq 250$  km from the trench). The stations are color-coded by the relaxation time inverted to fit each time series as in Figure A1. The stations colored in grey are those with not enough data to constrain the relaxation time, then the relaxation time of the nearest station is used to model the time series. The black curves are the modeled displacements using equation 3. The vertical grey line delineates the two studied periods: the short-term period (P1) from 3 days to 7 months after the mainshock and the long-term period (P2) from 7 months to 5.7 years after the mainshock. The map of the location of these stations can be found in Figure A1.



estimate the displacement offset. Such extrapolated displacements are plotted in cyan on the cross-section, while if data are available for the beginning and the end of the period, they are plotted in dark blue.

### 3.3 Complementarity and Correspondence between InSAR and GNSS observations

220 Both datasets bring complementary spatial and temporal information. GNSS time series provides continuous evolution of the position at precise points between the earthquake and 2022. Although the temporal sampling in InSAR is only 6 to 24 days, and the time series is noisier than GNSS, a post-seismic signal is clearly visible in the InSAR time series, and its amplitude can be extracted with great spatial coherency. InSAR data thus allow characterizing precisely the pattern of deformation and better locating the main features of the signal. Because the Sentinel-1 satellite was launched 7 months after the earthquake, the early  
225 stage of the post-seismic deformation cannot be assessed by InSAR. For GNSS, the period of observation varies depending on the stations and goes from the earthquake until 2022 for the most complete stations. Over the period covered by the InSAR time series (27 October 2014 to 31 December 2019), we compare the cumulative deformation obtained by InSAR and GNSS, with the GNSS displacements projected in the InSAR LOS. The Figure 2 shows that the same pattern is observed with both datasets, with a global coherency in the amplitude despite a few outliers (see also Figure A28 for further comparison of the  
230 amplitudes).

## 4 Modeling Strategy

### 4.1 Structure of the Model

To explore and model the trench perpendicular post-seismic displacements, we used a 2-dimensional Finite Element Model. We constructed the mesh with the software Coreform Cubit (2023) and computed the post-seismic relaxation and associated  
235 surface deformation with the Pylith 2.2.2 software (Aagaard et al., 2013, 2017) published under the MIT license. To align our 2D cross-section with the direction of maximum displacement, it is oriented with an angle of  $9^\circ$  with respect to the East which represents a medium angle between the East-West direction and the trench perpendicular direction. The section passes by the maximum of the mainshock co-seismic slip (Figure 1).

To avoid edge effects in the finite-element model, the section is 4000 km long: 1900 km on the oceanic side and 2100 km  
240 on the continental side and the depth is 1000 km. We use triangles to mesh the structure. Their size is increasing from the fault plane with a cell size of 5 km on the fault to 100 km on the model edges. The obtained model is composed of 13525 cells. The lateral sides are constrained with no displacement in the horizontal direction. The bottom has no vertical displacement. The surface is free to move.

The Central Andes exhibit a topographic variation of 13 km from the trench to the Western Cordillera (Armijo et al., 2015).  
245 Further inland, the Altiplano is characterized by a sustained high-elevation plateau of approximately 4000m. The Altiplano extends until it meets the Eastern Cordillera, where the topography gradually descends towards the Amazon basin. Our model



**Table 1.** Exploration of the parameters

Parameter	Name	Explored range	Optimal value
Afterslip depth	$A_d$	30 - 50 km	36 km
Afterslip width	$A_w$	16-28 km	24 km
Afterslip amplitude	$A_a$	0.3-0.5 m	0.4 m
Altiplano elastic thickness	$h$	10-35 km	25 km
Cold nose border	$d_{CN}$	80-95 km	84 km
Position of craton's border	$x_{craton}$	250-400 km	300 km
Oceanic viscosity	$\eta_{oc}$	$1.10^{20}$ - $5.10^{21}$ Pa.s	$1.10^{21}$ Pa.s
Continental viscosity	$\eta_{cont}$	$8.10^{18}$ - $5.10^{20}$ Pa.s	$3.10^{19}$ Pa.s
Maxwell weak zone viscosity	$\eta_{Mwz}$	$8.10^{18}$ - $5.10^{20}$ Pa.s	$2.10^{19}$ Pa.s
Kelvin weak zone viscosity	$\eta_{Kwz}$	$8.10^{17}$ - $5.10^{18}$ Pa.s	$2.10^{18}$ Pa.s

includes topography; we use the topography and the bathymetry of the global digital elevation model SRTM15+ (Tozer et al., 2019) (Figure 4A and C). The delimitation of the surface of the slab is taken from Slab2 from Hayes et al. (2018).

The model is composed of 5 domains (Figure 4): (1) An oceanic elastic layer, (2) an oceanic visco-elastic layer, (3) a continental elastic layer (including a cold nose and the craton), (4) a weak zone and (5) a continental visco-elastic layer.

In the following the structure of the different domains is detailed. The structural parameter explored are indicated in red in Figure 4 (Cold nose border  $d_{CN}$ , Altiplano elastic thickness  $h$ , position of craton's border  $x_{craton}$ ). The values given in the paragraph below correspond to the structure of our preferred model, and the range explored (if relevant) can be found in Table 1 and is detailed in section 4.3. Other structural parameters are fixed.

The oceanic elastic layer has a constant thickness of 60 km. The continental elastic layer has a variable thickness, with a maximum of 130 km. The continental elastic layer contains the cold nose (see section 1) from the trench until a vertical limit intercepting with the slab at a depth of  $d_{CN} = 84$  km in our best model. Wada and Wang (2009) explore the location of the decoupling depth between the cold nose, the slab and the mantle for several subduction zones with thermal modeling. They found a decoupling depth of  $\sim 80$  km in northern Chile at about  $23.5^\circ$ S of latitude. Our result is consistent with the value proposed by Wada and Wang (2009). Further inland, beneath the Altiplano, the elastic layer is thin ( $h = 25$  km, see section 2) and is underlaid by a region characterized by a low viscosity (weak zone). From  $x_{craton} = 300$  km to 600 km from the trench, there is a linear transition towards the thick craton (see section 2) which has a depth of 130 km. These two elastic layers have the same elastic parameters, given in Table 2. The weak zone, which strongly controls the post-seismic response of our models, is delimited by 3 geometrical parameters that are explored (see Figure 4 and Table 1): the border with the cold nose with the best value of  $d_{CN} = 84$  km on one side, the Altiplano elastic thickness with the best value of  $h = 25$  km, and the border with the craton that is a taper between  $x_{craton} = 300$  km and 600 km from the trench (for the best values). Below, the continental visco-elastic mantle is set at 130 km depth. The limits with the oceanic and continental visco-elastic mantles are respectively located below 60 km and 130 km.

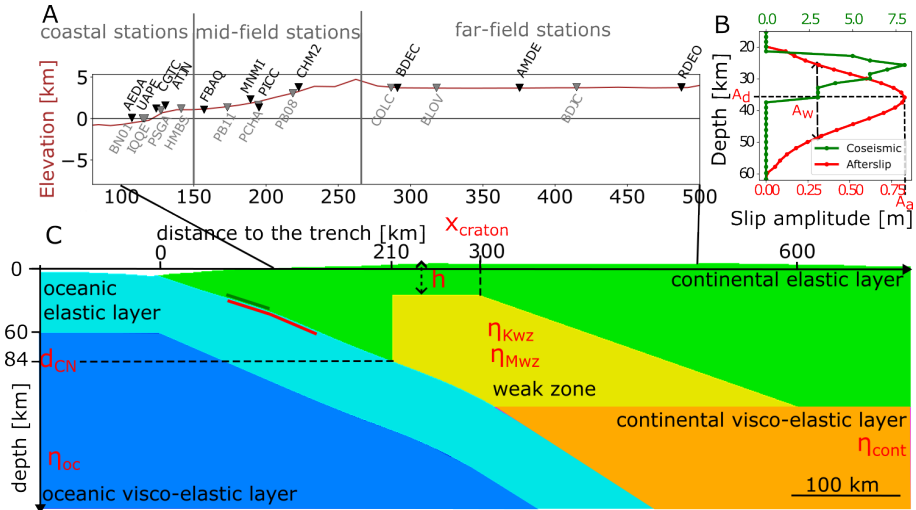


**Figure 4.** (A) Elevation along the cross section with the name of the different stations used in this study. The delimitation between coastal, mid-field and far-field stations is shown. (B) Co-seismic and afterslip amplitude along depth in green and red, respectively. The explored parameters of the afterslip are shown: the afterslip depth  $A_d$ , the afterslip amplitude  $A_a$  and the afterslip width  $A_w$ . (C) Structure of the model showing the 5 domains considered: the oceanic slab in light blue, the oceanic mantle in blue, the continental elastic layer in green, the weak zone in yellow and the continental mantle in orange. The parameters written in red are the ones that vary during this study. Along the slab, the green and red lines indicate the respective locations of the co-seismic and post-seismic slips imposed in our model (also detailed in (B)).

**Table 2.** Elastic parameters for the elastic and visco-elastic layers.  $\rho$ , designates the density,  $V_s$  the S-wave velocity,  $V_p$  the P-wave velocity,  $E$  the Young modulus,  $\mu$  the rigidity and  $\nu$  the Poisson’s coefficient.

Layer	$\rho$ ( $kg.m^{-3}$ )	$V_s$ ( $km.s^{-1}$ )	$V_p$ ( $km.s^{-1}$ )	$E$ (GPa)	$\mu$ (GPa)	$\nu$
Elastic	3320	4.2	8.0	150	59	0.3
Visco-elastic	3450	4.5	8.3	180	70	0.29

The model contains three visco-elastic domains. For the oceanic and continental visco-elastic layers we consider a Maxwell rheology while for the weak zone, the data require a transient relaxation time and we consider a Burgers rheology (see section 1). We transposed the Burgers viscosity and rigidity parameters into the generalized Maxwell formulation, which is implemented in Pylith (code available in the Appendix B1). The elastic parameters are given in Table 2 and the viscosities are in Table 3.



**Table 3.** Rheological properties of the different layers.  $\eta_M$  designates the Maxwell viscosity,  $\eta_K$ , the Kelvin viscosity and  $\mu_K$  the Kelvin rigidity.

Layer	Rheology	$\eta_M$ (Pa.s)	$\eta_K$ (Pa.s)	$\mu_K$ (GPa)
oceanic elastic	elastic	-	-	-
oceanic mantle	visco-elastic	$1.10^{21}$	-	-
continental elastic	elastic	-	-	-
weak zone	visco-elastic	$2.10^{19}$	$2.10^{18}$	136
continental mantle	visco-elastic	$3.10^{19}$	-	-

## 4.2 Modeling of the Displacement

275 We separate the modeling into two independent simulations: in the first one we model the co-seismic displacement field, stress, and consequent visco-elastic relaxation, and in the second one we model the afterslip with a kinematic approach. The final model and associated displacements correspond to the sum of the outputs from both models.

We first impose the co-seismic slip on the slab interface. Having an appropriate co-seismic model is crucial to model the subsequent post-seismic signal. Given the limited temporal resolution of our data, the co-seismic slip considered contains both the mainshock ( $M_w$  8.1) and its largest aftershock ( $M_w$  7.7) two days later. The slip distribution considered (see Figure 4B) is based on Jara et al. (2018). For the first simulation (co-seismic / visco-elastic), the co-seismic slip is imposed at the first time step. It induces a stress change in the medium that is relaxed over time. The modeled post-seismic deformation, extracted at the surface at the location of GNSS and/or InSAR points, is considered over the observation period of the data (from 3 days up to 5 years after the mainshock).

285 To model the afterslip, we use a simple approach and impose the spatio-temporal kinematic of the slip on the slab. The afterslip distribution as a function of depth  $A(z)$  has a Gaussian shape  $A(z) = \frac{G(z)}{\max(G(z))} \times A_a$  with  $G(z) = \frac{\exp(-(\frac{(z-A_d)^2}{2A_w^2}))}{\sqrt{2\pi} \times A_w}$  (see Figure 4B) where the afterslip amplitude  $A_a$ , its depth  $A_d$ , and the width of the afterslip zone  $A_w$  are among the parameters tested (Table 1). The temporal evolution of the afterslip is controlled by a logarithmic function:  $A(t, z) = A(z) \times \log(1 + \frac{t}{\tau_a})$ . The time constant  $\tau_a$  for the afterslip is set to 17 days, which corresponds to the time constant found when using equation (2) to model the time series for the stations closest to the trench, for which the afterslip can be considered as the dominant mechanism in the post-seismic phase.

## 4.3 Explored Parameters

Our modeling explores ten parameters (Table 1), which are detailed below. 3 parameters are associated with the afterslip, 3 with the structure of the weak zone and 4 parameters control the rheology of the visco-elastic regions.

295 We vary (1) the depth of maximum slip  $A_d$  between 30 to 50 km (2) the width of the Gaussian  $A_w$  between 16 and 28 km and (3) the amplitude of the slip  $A_a$  between 0.3 and 0.5 meters (see Figure 4B and Table 1). The amplitude  $A_a$  corresponds to



the maximum displacement after 7 months. The total displacement (after 6 years) is about twice the slip over the first 7 months. We initially set the afterslip values from the afterslip distribution of Hoffmann et al. (2018).

Three parameters correspond to the structure of the low-viscosity layer. (4) The thickness of the elastic layer under the altiplano  $h$  is varied from 10 to 35 km. (5) The position of the border between the elastic cold nose and the weak zone  $d_{CN}$ . It is constrained by the decoupling depth on the interface.  $d_{CN}$  is varied between 80 km and 95 km depth. The last structural parameter is (6) the border between the weak zone and the elastic craton, which is controlled by the position of the point  $x_{craton}$ , which is varied between 250 to 400 km from the Trench.  $x_{craton}$  marks the end of the flat upper limit of the weak zone. For  $x > x_{craton}$ , the depth of the weak zone increases with a constant slope, and the elastic craton becomes thicker. The weak zone terminates at a depth of 130 km, and a distance  $x_{craton} = 300$  km from the Trench.

The Maxwell viscosity of the oceanic visco-elastic layer (7)  $\eta_{oc}$  is explored between  $1 \times 10^{20}$  and  $5 \times 10^{21}$  Pa.s, the continental mantle (8)  $\eta_{cont}$  and the Maxwell weak zone (9)  $\eta_{Mwz}$  viscosities are tested between  $8 \times 10^{18}$  and  $5 \times 10^{20}$  Pa.s. On the low viscosity layer, (10) the Kelvin viscosity of the Burgers rheology  $\eta_{Kwz}$  is also varied between  $8 \times 10^{17}$  and  $5 \times 10^{18}$  Pa.s.

#### 4.4 Comparing Data and Models

To evaluate the range of model parameters that can adequately explain the observed surface displacements, we evaluate the misfit between our datasets and the model predictions. We then determine our preferred model and investigate the influence of each model parameter by varying the parameter ranges around the best model.

The evaluation of the agreement between observed surface displacement and model prediction is performed separately for GNSS and InSAR data. We first make visual comparisons between data and model over two observation periods: the short-term period (P1, from 3 days to 7.3 months), where only GNSS data are available, and the long-term period (P2, from 7.3 months to 5.72 years after the earthquake), where both GNSS and InSAR are available. The amplitudes of surface displacements along the profile for GNSS (horizontal and vertical, periods P1 and P2) and InSAR (Ascending and descending track, period P2), are shown in Figures 6 to 12, 14 and 15. These figures allow us to examine the spatial pattern of the model and the influence of the tested parameters on the modeled surface displacements.

We also make a quantitative evaluation of the fit between surface observations and models by computing the reduced Chi-Square for all datasets. For the GNSS data, the  $\chi_{GNSS}^2$  is computed from the displacement time series. For each time series  $i$ , the  $\chi_{iGNSS}^2$  is defined as

$$\chi_{iGNSS}^2 = \sum_{t=1}^{n_t} \frac{(d_{iGNSS}^{log}(t) - m_{iGNSS}^{log}(t))^2}{\sigma_{iGNSS}^2} \quad (4)$$

The global horizontal and vertical Chi squares are then computed by summing the estimations from individual stations with  $\chi_{HGNSS}^2 = \sum_{n=1}^{N_H} \chi_{iHGNSS}^2$  and  $\chi_{VGNSS}^2 = \sum_{i=1}^{N_V} \chi_{iVGNSS}^2$  where  $N_H$  and  $N_V$  are the number of horizontal and vertical time series. The uncertainties for each station  $i$  are estimated based on the dispersion (RMS) of the data around the post-seismic time series fit from equation 3:  $\sigma_{iGNSS} = 3 \times RMS_{i_{best}}$ .



For the InSAR data, since the time series is noisy, the comparison between data and model is made directly on the estimation  
330 of the amplitude over the observation period. The cumulative InSAR displacement (in the radar LOS) over the observation  
period (Figure 2) is estimated for each pixel from the trajectory model of equation 1. We then subsample the InSAR map,  
considering  $N_I$  InSAR points located every 10 km along the cross-section. The subsampled displacements  $d_{iInSAR}$  are the  
median values across the 100 km wide section, and  $\sigma_{iInSAR}$  is 1.4826 times the median absolute deviation (see grey dots and  
shaded grey region in the profiles E and F in Figures 6 to 15).

335 For each InSAR track, we evaluate the adjustment between the data  $d_{iInSAR}$  and the model  $m_{iInSAR}$  (modeled surface  
displacements projected in the radar LOS) by:

$$\chi_{InSAR}^2 = \frac{1}{N_I} \frac{\sum_{i=1}^{N_I} (d_{iInSAR} - m_{iInSAR})^2}{\sigma_{InSAR}^2} \quad (5)$$

The influence of the horizontal and the vertical on the InSAR displacements depends on the LOS of the acquisition. The  
InSAR is more sensitive to the vertical component bringing then another way to measure vertical displacements. For the  
340 horizontal component, it is more sensitive to the East-West displacements almost ignoring the North-South one.

In the following, we evaluate the influence of the different model parameters. In Figures 7 to 15, we compare observed  
surface displacements to model predictions along cross-sections at a short time scale (subplots A and B, GNSS data only), and  
a longer time scale (subplots C and D for GNSS, F and G for InSAR), and also by evaluating the variation in  $\chi^2$  with model  
parameters (subplots E) for horizontal ( $\chi_{HGNS}^2$ ) and vertical ( $\chi_{VGNS}^2$ ) GNSS and ascending ( $\chi_{AInSAR}^2$ ) and descending  
345 ( $\chi_{DInSAR}^2$ ) InSAR tracks.

## 5 Results

### 5.1 Evidence of for the Need for Both Processes: Afterslip and Visco-elastic Relaxation

The GNSS time series (Figure 3) shows that on average, the time constant associated with the post-seismic deformation tends to  
increase with increasing distance from the trench: the mean time constant, when estimated over the complete 8-year time series,  
350 is 17 days for coastal stations and up to 31 days in Bolivia. These variations indicate that different processes are combined  
at different spatial and temporal scales in the post-seismic signal. To decipher between these processes, we consider that at a  
short time scale, and close to the earthquake rupture, afterslip must be the dominant mechanism and thus explain most of the  
observed signal. The afterslip is a relaxation phenomenon of the fault plane that surrounds the co-seismic slip. It mostly impacts  
the coastal stations that are the nearest to the fault interface. Instead, the visco-elastic relaxation is happening in the mantle and  
355 in the weak zone and has a spatial signature with a large wavelength. That is why at the trench, the displacement observed is  
mainly due to the afterslip. We use the average time constant of the coastal stations (AEDA to HMBS)  $\tau_{afterslip} = 17$  days to  
constrain the evolution of the afterslip.

The respective contribution of afterslip and visco-elastic deformation for our best model (see below for the justification of  
model parameters) is shown in Figure 5 for the temporal evolution along with GNSS time series, and in Figure 6 for the spatial



360 signal along a cross-section. We see that afterslip (green curve) is the dominant process at a short time scale during the months following the earthquake (Figure 6A and B) and that its contribution is dominant mostly at coastal stations (e.g. PSGA and ATJN in Figure 5). Over a longer time scale (Figure 6 C, D, E, F), and in the far-field (e.g. COLC and BDJC in Figure 5), visco-elastic relaxation (blue curve) becomes significant. We can observe that although the contribution of afterslip and visco-elastic deformation add up on the horizontal component (Figure 6 A and C), they can produce deformation of opposite signs  
365 on the vertical (Figure 6 B and D). Thus visco-elastic deformation is needed to explain the observed uplift pattern. Due to the differences in acquisition geometry, the ascending track is more sensitive to the visco-elastic deformation than the descending track which is more sensitive to afterslip (Figure 6 E and F). InSAR data computed on both ascending and descending tracks are therefore useful to help discriminate between the different processes.

## 5.2 Afterslip

370 In section 5.1, we show that the afterslip is predominant at short time scales (a few months), and we have set its temporal evolution (logarithmic decay with a time constant of 17 days) so that it reproduces the observed displacement at the coastal stations. The depth of the afterslip ( $A_d$ ) mostly induces a horizontal offset of the modelled curve in near field ( Figure B2). The width of the afterslip pulse ( $A_w$ ) (Figure B3) as well as the maximum slip value ( $A_a$ ) (Figure B4) control the amplitude of the surface displacements associated with afterslip. Best fitting parameters are  $A_w = 24$  km and  $A_a = 0.4$  m, more results  
375 are detailed in the Appendix B. Our optimal afterslip model, presented in Figure 4B, gives a maximum slip at a depth  $A_d = 36$  km, it is located below the co-seismic slip (which extends between 22 and 34 km depth). Some afterslip overlaps up-dip with the co-seismic slip, and it extends downdip down to 60 km depth.

## 5.3 Structure

We then investigate how our data bring constraints on the structure and rheology of the crust and upper mantle, and more  
380 precisely on the weak zone beneath the Altiplano. Here, we explore how the geometry of this weak zone influences the modeled displacements at the surface. The rheological parameters correspond to our best model and are not varied. Their influence is discussed in the next section. Geophysical studies and thermo-mechanical models give some constraints on the thickness of the elastic layer  $h$  beneath the Altiplano. In our models, we varied  $h$  between 10 and 35 km, and as expected, we observe that a thicker elastic crust produces surface displacement of longer wavelength and lower amplitudes. We find an optimal value  
385 for  $h = 25$  km (Figure 7) which gives the best compromise in fitting the GNSS components together with both InSAR tracks. This thickness is compatible with the values found in the literature for thermo-mechanical models (Araya Vargas et al., 2021; Springer, 1999).

We then studied the lateral extension of the weak zone across the Altiplano: we vary the position of its limit trenchward which is constraints by its depth ( $d_{CN}$ , marking the downdip end of the elastic cold nose). Its inland limit gradually deepens  
390 over 300 km, and we varied the position  $x_{craton}$  that marks the beginning of the thickening of the elastic crust at the transition with the Brazilian craton. The cold nose limit controls the position of the maximum uplift pattern seen in the vertical component (Figure 8). The ascending InSAR track brings the strongest constraint on the optimal location of the cold nose limit ( $d_{CN} = 84$

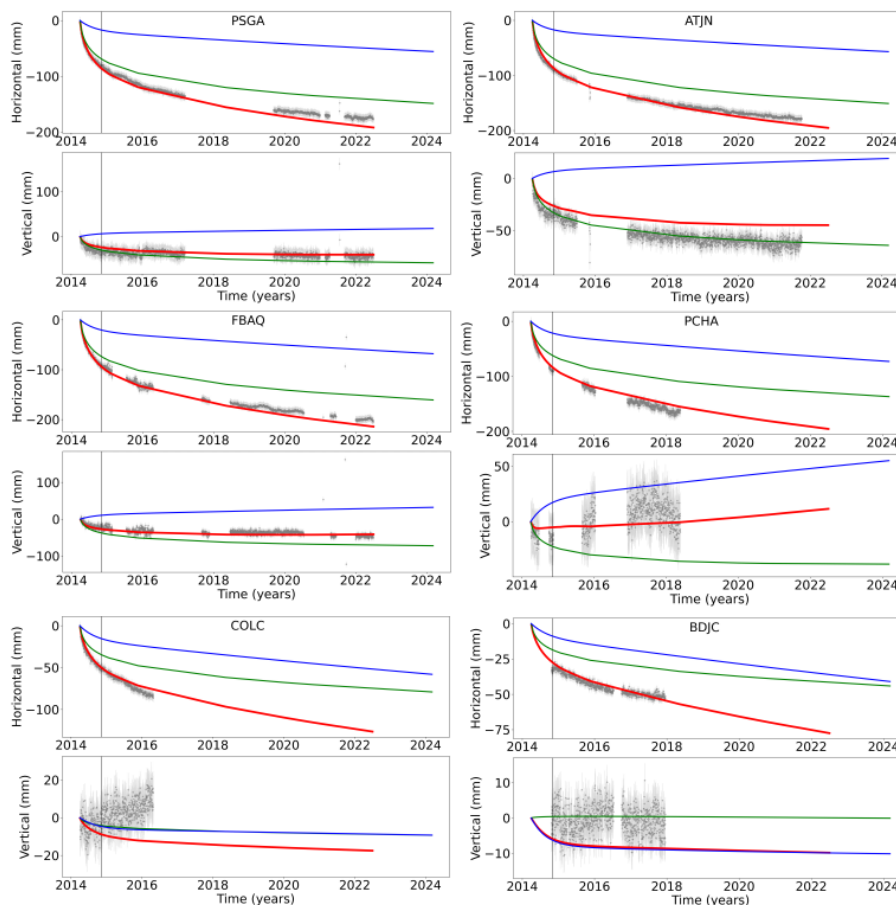


**Figure 5.** Temporal evolution of the post-seismic displacements and predictions of the best model for coastal stations (PSGA and ATJN), intermediate-field stations (FBAQ and PCHA) and far-field stations (COLC and BDJC). For each station, the top subplot shows the horizontal displacement and the bottom one, the vertical displacement. Grey dots with error bars show the GNSS data with the associated uncertainties. The colored lines are the modeled displacements: the blue curve is the visco-elastic contribution and the green curve is the afterslip contribution. The red curve is the total modeled displacement, combining afterslip and visco-elastic displacements. The best model parameters are presented in the table 1.

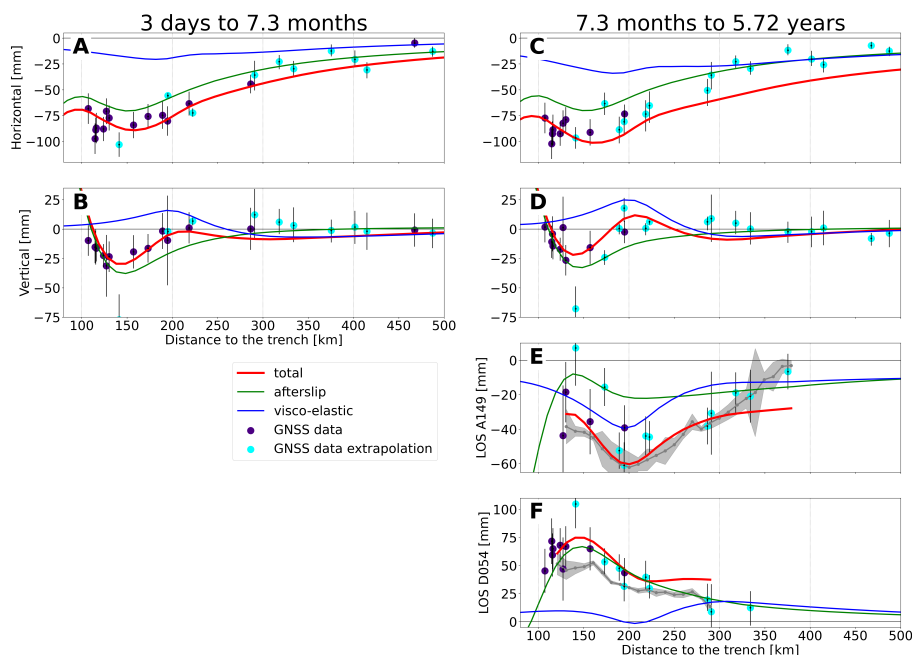


**Figure 6.** Cross section of the best model along with GNSS and InSAR data for different periods. On all plots, the x-axis is the distance from the trench along the section. The green, blue and red curves represent respectively the afterslip, visco-elastic and total displacement predicted by the best model. Subplots A and B represent respectively the horizontal and vertical cumulative displacement in millimeters from 3 days to 7.3 months. Subplots C, D, E and F represent respectively the horizontal, vertical, LOS of the InSAR track A149 and LOS of the InSAR track D054 cumulative displacement in millimeters from 7.3 months to 5.72 years. Dark blue points represent the displacement extracted from the data with the associated error bars. Cyan points represent the displacement extrapolated from the trajectory model fit for the time series with missing data (Figure 3). Subplots E and F are the cumulative InSAR displacement from 7.3 months to 5.72 years after the earthquake, in the Radar LOS for the tracks A149 and D054 respectively. The grey curve represents the median value of the InSAR and the grey envelope, 1.4826 times the median absolute deviation.

km). Note that a model without cold nose does not produce vertical uplift, as already discussed by Luo and Wang (2021a), and would thus not fit the data. Varying the landward limit of the low-viscosity zone will affect the amplitude and shape of the post-seismic relaxation in the intermediate and far-field, a shorter weak zone inducing smaller displacements (Figure 9). We find an optimal position of  $x_{craton} = 300$  km, which makes the shallow section of the weak zone 90 km wide below the Altiplano before it starts to deepen.

#### 5.4 Rheology

We finally investigate the influence of rheological parameters, in the weak zone as well as in the oceanic and continental mantles. The tests made with variable viscosity in the oceanic mantle show its influence on the modeled displacements near the trench. They show that no significant visco-elastic relaxation in the oceanic mantle during the observation period is required to

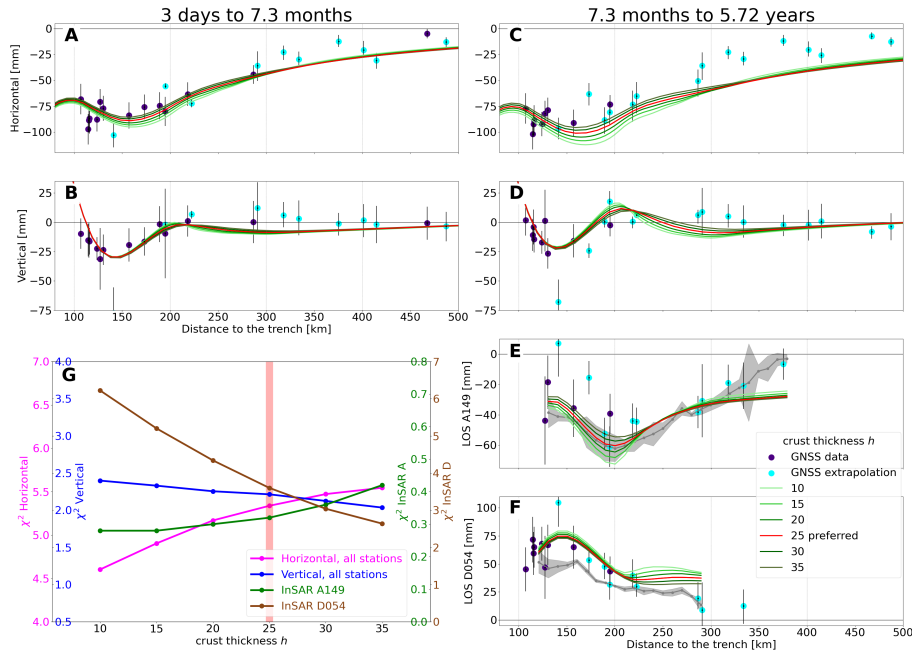


**Figure 7.** Exploration of the elastic layer thickness  $h$ . The subfigures A, B, C, D, E and F show the same organization as in figure 6. (G) draws the evolution of the different  $\chi^2$  with the tested parameter. The pink curve corresponds to the horizontal  $\chi^2$ , the blue curve to the vertical  $\chi^2$  and the green curve to the  $\chi^2$  of the InSAR A149. The scale changes following the component. An elastic layer thickness  $h = 25$  km best fits the pattern observed in the data.

fit the data. We select  $\eta_{oc} = 10^{21}$  Pa.s (i.e. quasi-elastic behaviour during the observation period, with a relaxation time of 450 years), lower viscosity values inducing a significant misfit to the coastal stations and near-field ascending InSAR track (Figure 10). The viscosity of the continental mantle influences the amplitude of the intermediate and far-field displacements over the period P2 (Figure 11). We set  $\eta_{cont} = 3 \times 10^{19}$ , a value that captures the amplitude of the horizontal and vertical deformation in the intermediate-field, while also providing a reasonable fit to the far-field data.

The rheological properties in the weak zone are tested in Figures 12 to 15. First, we tested the rheological law that controls the propagation of the deformation in the medium. We tried the Maxwell and the Burgers rheologies. The Burgers rheology is the combination of a Maxwell body and a Kelvin body. It allows for a transient relaxation at smaller characteristic times. In Figure 13, we see that during the first year, there is a lack of displacements using the Maxwell rheology while the Burgers rheology fits the temporal evolution for the first year and in the longer term. Spatially, at short-time scales (Figure 12A and B), we see more effects due to the visco-elasticity. It improves the fit on the vertical because the afterslip leads to too much subsidence between 150 and 300 km, the visco-elastic relaxation produces uplift, then it compensates the afterslip and the data are well fitted using a Burgers rheology.

The data fit is thus significantly improved by considering a Burgers rheology instead of a Maxwell rheology in the weak zone. The parameters of this Burgers rheology have been investigated in Figure 14 (viscosity  $\eta_{M_{wz}}$  of the Maxwell component in

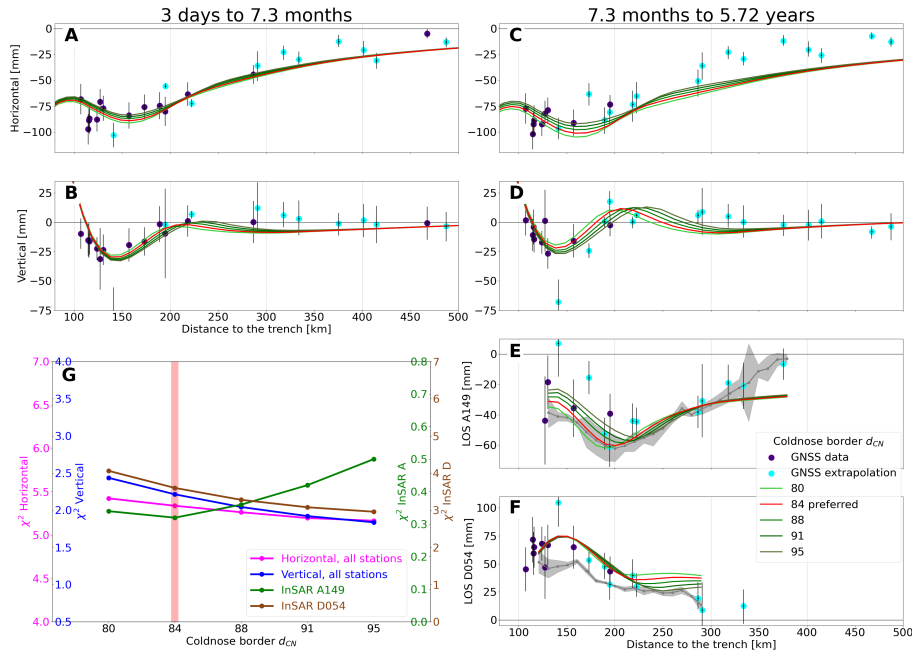


**Figure 8.** Variation of the cold nose border  $d_{CN}$ . The subfigures A, B, C, D, E and F show the same organization as in figure 6. (G) shows the same organization as in figure 7. The limit between the cold nose and the weak zone at  $d_{CN} = 84\text{km}$  depth best fits the pattern observed in the vertical displacements and on the track A149.

the Burgers rheology), and Figure 15 (viscosity  $\eta_{K_{wz}}$  of the Kelvin component of the Burgers rheology). Varying the Maxwell viscosity will mostly control the amplitude of the visco-elastic deformation pattern over the period P2 (long time scale). We find an optimal value of  $\eta_{M_{wz}} = 2 \times 10^{19}$  Pa.s that provides the best fit to the vertical GNSS data and InSAR Ascending track 420 (Figure 14 D and E). Changing the viscosity of the Kelvin element will affect both periods (P1 and P2), and mostly vary the amplitude (Figure 15). We select  $\eta_{K_{wz}} = 2 \times 10^{18}$  Pa.s, 10 times smaller than the Maxwell viscosity which is typical for visco-elastic simulations incorporated Burgers rheologies (Luo and Wang, 2021a).

## 6 Discussion

### 6.1 Limitations of the model

425 Models are simplifications of natural processes. Our models involve important limitations. First, we exclude gravitational body forces in our viscoelastic simulations. Including gravity often prevents the system from reaching a stable initial state, as the model continues to relax under its own weight (Aagaard et al., 2017). To avoid this numerical instability and ensure consistency across all simulations, gravity is omitted. Second, we make a 2D simplification of a 3D process and we use a simplified structure below the Andes. This was done on purpose to meet the objective of the study : assess the geometry of the weak zone and its

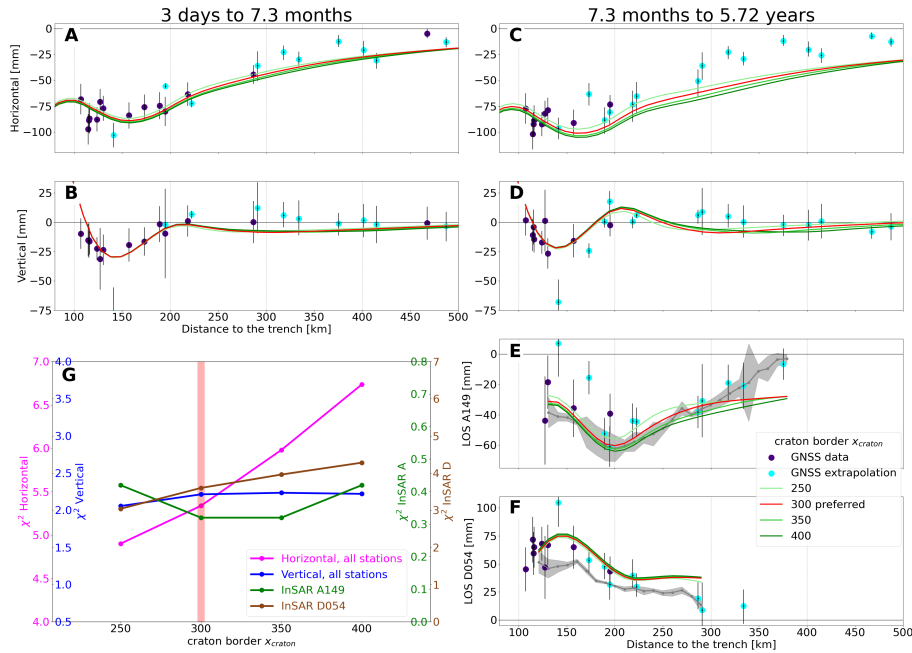


**Figure 9.** Exploration of the craton border  $x_{craton}$ . The subfigures A, B, C, D, E and F show the same organization as in figure 6. (G) shows the same organization as in figure 7. A limit between the craton and the weak zone at  $x_{craton} = 300\text{km}$  from the trench along the x-axis fits the best the pattern observed in the data.

430 rheology over the decadal time scale by performing a parametric exploration. Like in any parametric model, it is necessary  
to limit the amount of variables to be explored, and a simplified geometry avoids having to explore too many trade-offs. A  
model meant to reproduce the full 3D displacement field would definitely require a 3D geometry. However previous studies  
have shown that to assess the trench perpendicular structure, such as the cold nose or the transition between the weak zone  
and the craton, a 2D assumption provides reasonable results, comparable to 3D simulations at the first order (Luo and Wang,  
435 2021b, 2022). The other important result from our study is the necessity of using a Burgers rheology in the weak zone to  
explain the temporal evolution of afterslip versus visco-elastic in near field versus far field. As this is mostly constrained by the  
relative amplitude of the measured signal, using a 2D model should not introduce a strong bias.

## 6.2 Influence of Rheological Discontinuities in the Vertical Displacement Field

440 Previous studies on the post-seismic deformation following the Iquique earthquake exhibit a significantly larger misfit in the  
vertical component compared to the horizontal component (Hoffmann et al., 2018; Hu et al., 2021). The vertical component  
presents higher uncertainties and is then generally less well reproduced for the benefit of the horizontal component. Therefore,  
vertical displacements are better defined when multi-year time windows are analyzed, as in this work. The visco-elastic re-  
laxation has a strong influence on the vertical component (Li et al., 2017; Luo and Wang, 2021a) and some of the parameters

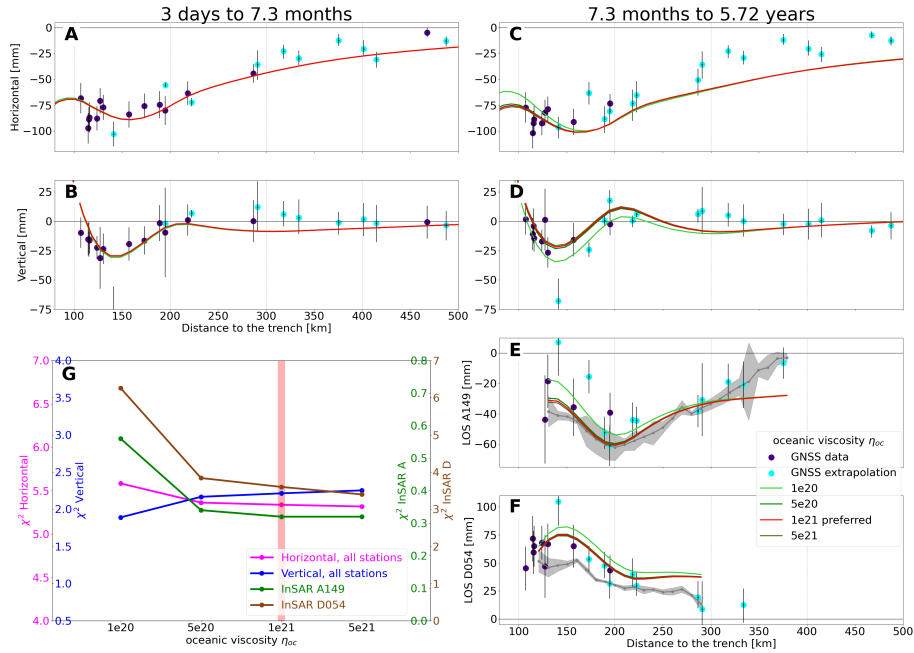


**Figure 10.** Exploration of the oceanic viscosity  $\eta_{oc}$ . The subfigures A, B, C, D, E and F show the same organization as in figure 6. (G) shows the same organization as in figure 7. An oceanic viscosity  $\eta_{oc} = 1.10^{21} Pa.s$  best fits the pattern observed in the data.

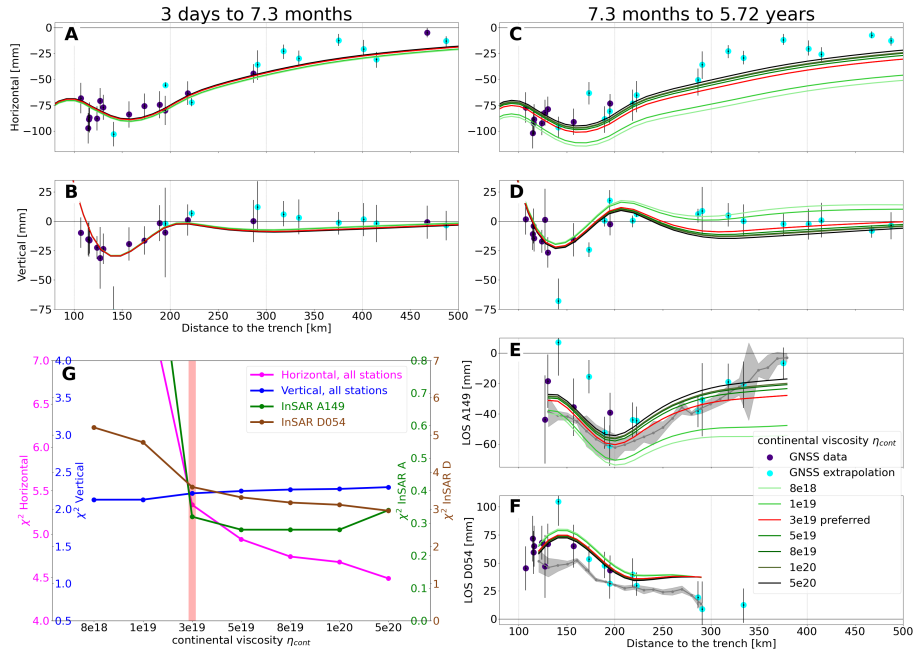


**Figure 11.** Exploration of the continental viscosity  $\eta_{cont}$ . The subfigures A, B, C, D, E and F show the same organization as in figure 6. (G) shows the same organization as in figure 7. A continental viscosity of  $\eta_{cont} = 3.10^{19} Pa.s$  best fits the pattern observed in the data.

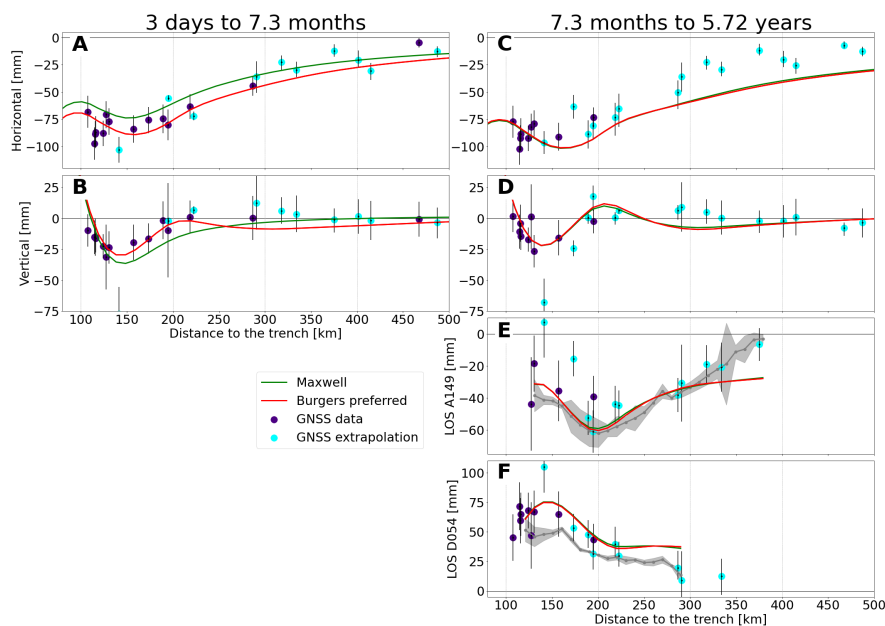


**Figure 12.** Comparison between Maxwell and Burgers rheologies in the weak zone. The organization of the figure follow the one of the 6. Here the curves are color-coded the same way as in the figure 13. The red curve is the best model and the green curve represents a model with a Maxwell instead of a Burgers rheology in the weak zone.

we have explored can only be assessed by looking at the vertical deformation ( $d_{CN}$ ,  $\eta_{oc}$ ,  $\eta_{M_{wz}}$ ). In particular, the inclusion of InSAR data in this study allows us to better constrain the vertical deformation, as InSAR data are highly sensitive to the vertical component. The data used therefore enable us to better explore these processes. The evolution of the misfit on the horizontal and the vertical for a given parameter is often opposed. But it is possible to reconcile them. Notably, the addition of a cold nose together with a weak zone is necessary to reproduce the observed vertical displacement field. The addition of a Burgers rheology allows to predict a different pattern at short time scale and allows to fit the early uplift on the Altiplano (Figures 12 and 13).

### 6.3 Far-field Subsidence

The post-seismic deformation following large subduction earthquakes shows far-field subsidence and was already described for the  $M_w$ 8.8 Maule earthquake (Li et al., 2017) or the  $M_w$ 9.1 Tohoku Oki earthquake (Li et al., 2020). This pattern is of low amplitude and long wavelength. In this study, it is not clear if a far-field subsidence is seen or not. The Bolivian far-field data are affected by high uncertainties due to the lack of data before the Iquique earthquake and several data gaps. Indeed, most stations in Bolivia start to register only  $\sim$ 6 months after the earthquake, and only 2 or 3 years of data are available. We therefore have to extrapolate the post-seismic displacements using a model assuming a given interseismic velocity, that

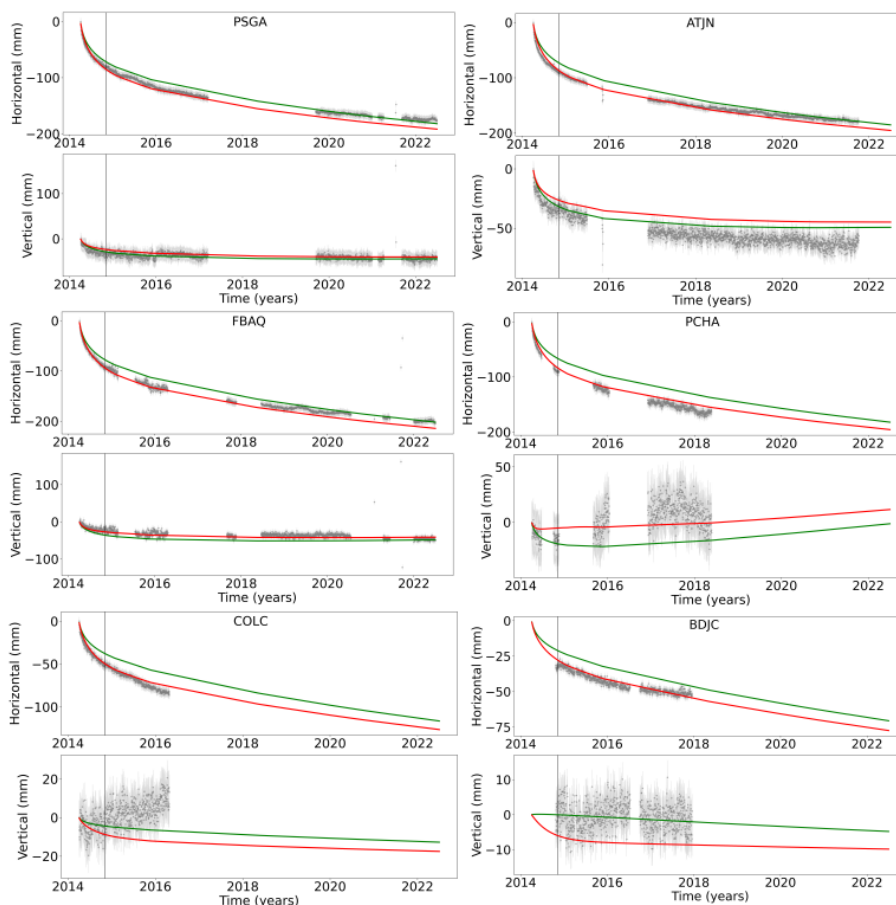


**Figure 13.** Temporal evolution of the post-seismic displacements at coastal stations (PSGA and ATJN), intermediate-field stations (FBAQ and PCHA) and far-field stations (COLC and BDJC). For each station, the top subplot shows the horizontal displacements and the bottom one, the vertical displacements. Grey dots with lines show the GNSS data with the associated uncertainties. The red curve shows the best model with a Burgers rheology in the weak zone. The green curve shows the model with a Maxwell rheology instead of a Burgers in the weak zone.

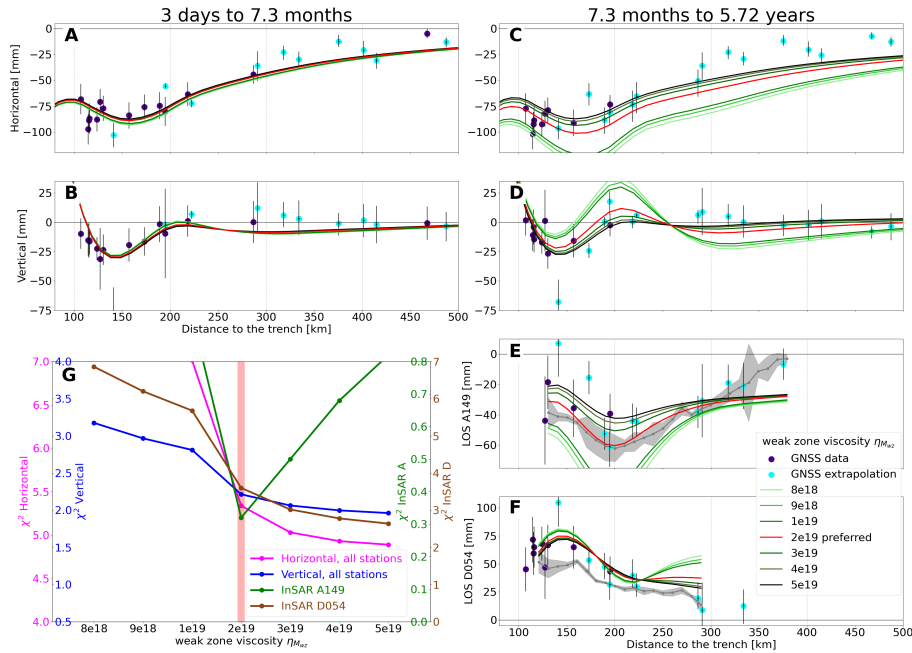


**Figure 14.** Exploration of the Maxwell viscosity  $\eta_{M_{wz}}$  in the weak zone. A lower viscosity induces more displacement. It impacts mainly the long-term period. The subfigures A, B, C, D, E and F show the same organization as in figure 6. (G) shows the same organization as in figure 7. A Maxwell viscosity for the weak zone of  $\eta_{M_{wz}} = 2.10^{19} Pa.s$  best fits the pattern observed in the data.

likely propagates uncertainties. Since the InSAR time series is flattened on the GNSS displacements, any reference issue in the GPS will propagate in the InSAR flattening (a ramp correction that does not affect the pattern of deformation). These large  
 460 uncertainties in the eastern side of our data set, make it difficult to decipher between zero displacement and small subsidence. If a subsidence exists, its amplitude is very low. The amplitude of the far-field subsidence may be linked with the magnitude of the earthquake. As the magnitude of the Iquique earthquake is lower ( $M_w 8.1$ ) than the Maule or Tohoku earthquakes, it may imply an amplitude of subsidence that is small and close to the limit of detection.

#### 6.4 Structure of the Weak Zone

465 The final model obtained contains a weak zone below the Western cordillera between 210 km and 300 km from the trench, which progressively deepens under the Altiplano. The extent of the weak zone corresponds to the high topography of the Andes and the associated crustal root that is particularly deep in this region. The boundary between the cold nose and the weak zone represents the depth of decoupling between the slab and the overriding plate. Above, the plates are decoupled, below plates are viscously coupled and the the slab drags the continental plate at depth. It creates a flow and this region is hot enough  
 470 for partial melting. This is not the case above the decoupling depth where there is no flow and the region is then colder. The depth of decoupling has been studied by Wada et al. (2008) and Wada and Wang (2009). They found a depth of  $\sim 80$  km.

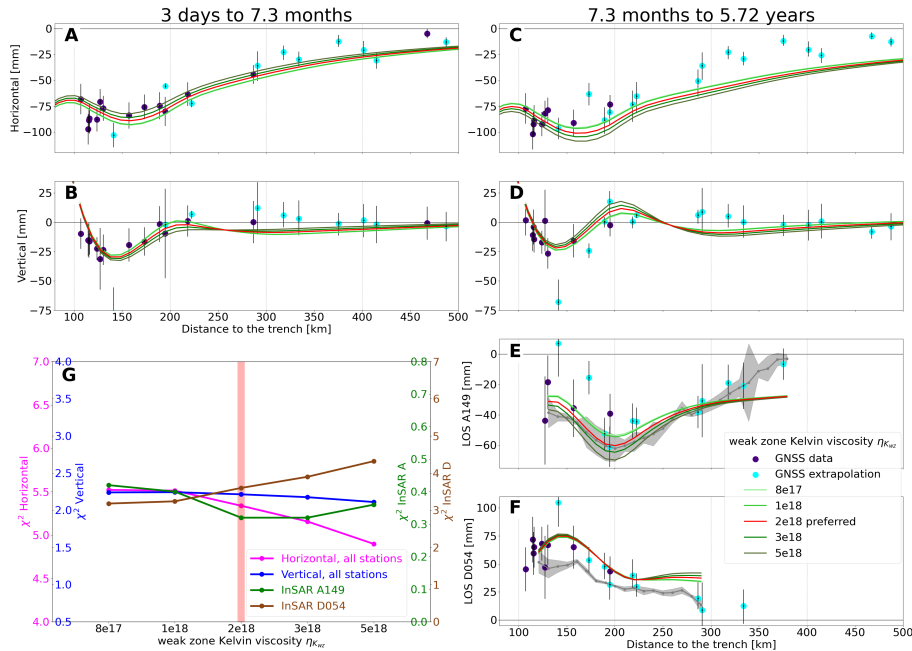


**Figure 15.** Exploration of the Kelvin viscosity  $\eta_{K_{wz}}$  in the weak zone. The subfigures A, B, C, D and E show the same organization as in figure 6. (G) shows the same organization as in figure 7. A Kelvin viscosity for the weak zone of  $\eta_{K_{wz}} = 2.10^{18} Pa.s$  best fits the pattern observed in the data.

Our preferred model shows a decoupling depth of 84 km which is close to the one found by Wada and Wang (2009). The heat flow from the thermo-mechanical model is not well constrained in northern Chile because of few measurements in that region. At depth, this weak zone extends from 25 km depth (corresponding to the thickness of the elastic Altiplano) down to 130 km depth. At greater depths, the visco-elastic continental mantle takes over. The weak zone is located down dip the volcanic arc. A weak viscosity in this area is expected due to increased temperature and hydration causing partial melting below the arc. This weak zone indeed corresponds to a hotter area following temperature models (Araya Vargas et al., 2021; Springer, 1999) from 210 km from the trench and diminishing progressively from 300 km. It is also confirmed by the presence of hydrated phases imaged by magneto-telluric data (Araya Vargas et al., 2019) and seismic (Gao et al., 2021; Yuan et al., 2000). In our model, the border between the low-viscosity area and the craton is modeled by a slope. This is a way to represent the variation of the viscosity. As shown by the temperature models by Araya Vargas et al. (2021) and Springer (1999), the temperature slowly diminishes, implying that the viscosity may also slowly increase in the eastern part of the Altiplano. The two limits of the taper may therefore rather represent the viscosity gradient than an actual geometry.



## 7 Conclusions

485 To fit the post-seismic surface displacements of the 2014  $M_w$ 8.1 Iquique earthquake, we use a model that includes a weak zone beneath the Altiplano. In the corner of the continental mantle, elastic behavior of the cold nose is required to produce the uplift seen at the surface. Further east, the weak zone, extends from 210 km from the trench at a depth of 25 km and deepens at 300 km. This region behaves as a Burgers rheology with a Maxwell viscosity of  $2 \cdot 10^{19}$  Pa.s and a transient Kelvin viscosity of  $2 \cdot 10^{18}$  Pa.s. The exploration of the viscosities shows that the viscosity of the continental mantle is lower than that of the  
490 oceanic mantle, the latter being so high that it does not relax in the 8-year period considered.

InSAR data brings spatial continuity to the dataset. While GNSS data are available at some points only, InSAR continuously covers a region and brings consistency to the displacement pattern. It allows us to better define the pattern observed: what is the shape, the extent and the location of the post-seismic deformation, which is in direct link with the underlying structure. In addition, it provides useful constraints on the vertical component with lower uncertainties than the GNSS data. The InSAR  
495 tracks cover the Altiplano above the weak zone and all the uplift area, which allows to point the location of the maximum uplift and how it diminishes.

Our preferred model incorporates a cold nose, this near trench elastic area predicted by thermal models (Wada and Wang, 2009) governs the displacements observed above that region because it drives the mantle flow at the border with the weak zone. The transition from elastic to visco-elastic with a low viscosity creates an uplift above the boundary. Without this cold nose  
500 we would be unable to reproduce the observed uplift pattern with the model. The modeling performed here shows that surface displacements can only be matched with the presence of this rheological contrast, confirming the need for a cold nose derived from thermo-mechanical behaviour. The cold nose ends with the decoupling depth which allows the mantle below to flow and react visco-elastically.

We show that below the western part of the Altiplano, the viscosity should be low ( $\eta_{M_{wz}} = 2 \cdot 10^{19}$  Pa.s). This is required  
505 by the amplitude of the uplift pattern over this area. The location is well resolved thanks to the InSAR data. The location is in good agreement with the Andean structure. The western boundary correlates with the western cordillera hosting the volcanic arc. This weak zone therefore correlates with the place of melting of the magma, which should be characterized by a lower viscosity due to partial melting.

Another key point demonstrated by this study is the need to use a Burgers rheology instead of a Maxwell rheology within  
510 the weak zone. Our data require the need for a transient viscosity to fit the vertical pattern observed at short time scales, i.e. during the months following the earthquake. During this period, we need a combination of afterslip on the fault plane and visco-elastic relaxation at short time scales to explain the pattern and amplitude of the vertical displacements. Also, we can see in the time series, but also by comparing the early and late periods on the sections, that by fitting the long-term displacements with a Maxwell rheology, there is a lack of amplitude due to the visco-elasticity in the early stage. The continental mantle is too  
515 deep (below the weak zone) to affect the surface data or is further east where the data quality is lower. The viscosity required in the oceanic mantle is high enough that the characteristic time is higher than the time span of this study. That is why, the use of



a Burgers rheology will not affect the results. The temporal evolution of the deformation therefore requires a Burgers rheology rather than a Maxwell rheology in the weak zone below the Altiplano.

*Code and data availability.* All time series used in this manuscript is available at [https://doi.osug.fr/public/GNSS\\_products/GNSS.products.SouthAmerica\\_GIPSYX.daily.html](https://doi.osug.fr/public/GNSS_products/GNSS.products.SouthAmerica_GIPSYX.daily.html). RINEX data from CSN network are available at <http://gps.csn.uchile.cl> RINEX data from Bolivia are available from UNAVCO at <https://www.unavco.org/data/doi/10.7283/T5DJ5D0X> RINEX data from RBMC are available at <https://www.ibge.gov.br/en/geosciences/geodetic-positioning/geodetic-networks/19213-brazilian-network-for-continuous-monitoring-of-the-gnss-systems.html?=&t=downloads>. The trajectory model software (ITSA) is available at <https://gricad-gitlab.univ-grenoble-alpes.fr/isterre-cycle/itsa>. SAR Sentinel-1 data are available at <https://peps.cnes.fr/rocket/#/home> or <https://scihub.copernicus.eu/>. Pylith software is available at <https://geodynamics.org/resources/pylith>.

*Acknowledgements.* This work was supported by funding from the European Research Council (ERC) CoG 865963 DEEP-trigger. Most computing was made on the CIMENT/GRICAD infrastructure (<https://gricad.univ-grenoble-alpes.fr>). TEXT

*Author contributions.* JC analysed the GNSS and InSAR time series, did the modelling and wrote the first draft of the manuscript, MR supervised the work and participated in the modelling, MPD did the InSAR processing and supervised the work, MM MM participated in the modelling, FH participated in the InSAR analysis, ATT and GJ processed the GNSS data, JCB acquired the GNSS data, AT participated in the discussion and structural interpretation, AS obtained the funding, conceptualized and supervised the work, participated in GNSS data acquisition and processing, all authors participated in the discussion and in the writing of the manuscript

*Competing interests.* The authors declare no competing interests.



## References

- 535 Aagaard, B., Knepley, M., and Williams, C.: A domain decomposition approach to implementing fault slip in finite-element models of quasi-static and dynamic crustal deformation, *Journal of Geophysical Research: Solid Earth*, 118, 3059–3079, <https://doi.org/10.1002/jgrb.50217>, 2013.
- Aagaard, B., Knepley, M., and Williams, C.: PyLith v2.2.2 [Computer software], *Computational Infrastructure for Geodynamics*, <https://doi.org/10.5281/zenodo.438705>, 2017.
- 540 Altamimi, Z., Rebischung, P., Métivier, L., and Collilieux, X.: ITRF2014: A new release of the International Terrestrial Reference Frame modeling nonlinear station motions, *Journal of Geophysical Research: Solid Earth*, 121, 6109–6131, <https://doi.org/10.1002/2016JB013098>, 2016.
- Araya Vargas, J., Meqbel, N. M., Ritter, O., Brasse, H., Weckmann, U., Yáñez, G., and Godoy, B.: Fluid Distribution in the Central Andes Subduction Zone Imaged With Magnetotellurics, *Journal of Geophysical Research: Solid Earth*, 124, 4017–4034, <https://doi.org/10.1029/2018JB016933>, 2019.
- 545 Araya Vargas, J., Sanhueza, J., and Yáñez, G.: The Role of Temperature in the Along-Margin Distribution of Volcanism and Seismicity in Subduction Zones: Insights From 3-D Thermomechanical Modeling of the Central Andean Margin, *Tectonics*, 40, 1–20, <https://doi.org/10.1029/2021TC006879>, 2021.
- Arcay, D., Tric, E., and Doin, M.-P.: Numerical simulations of subduction zones: Effect of slab dehydration on the mantle wedge dynamics, *Physics of the Earth and Planetary Interiors*, 149, 133–153, 2005.
- 550 Armijo, R., Lacassin, R., Coudurier-Curveur, A., and Carrizo, D.: Coupled tectonic evolution of Andean orogeny and global climate, *Earth Science Reviews*, 143, 1–35, <https://doi.org/10.1016/j.earscirev.2015.01.005>, 2015.
- Babeyko, A. Y., Sobolev, S. V., Trumbull, R. B., Oncken, O., and Lavier, L. L.: Numerical models of crustal scale convection and partial melting beneath the Altiplano-Puna plateau, *Earth and Planetary Science Letters*, 199, 373–388, [https://doi.org/10.1016/S0012-821X\(02\)00597-6](https://doi.org/10.1016/S0012-821X(02)00597-6), 2002.
- 555 Béjar-Pizarro, M., Carrizo, D., Socquet, A., Armijo, R., Barrientos, S., Bondoux, F., Bonvalot, S., Campos, J., Comte, D., De Chabaliér, J., et al.: Asperities and barriers on the seismogenic zone in North Chile: state-of-the-art after the 2007 M w 7.7 Tocopilla earthquake inferred by GPS and InSAR data, *Geophysical Journal International*, 183, 390–406, 2010.
- Béjar-Pizarro, M., Socquet, A., Armijo, R., Carrizo, D., Genrich, J., and Simons, M.: Andean structural control on interseismic coupling in the North Chile subduction zone, *Nature Geoscience*, 6, 462–467, 2013.
- 560 Bertiger, W., Bar-Sever, Y., Dorsey, A., Haines, B., Harvey, N., Hemberger, D., Heflin, M., Lu, W., Miller, M., Moore, A. W., Murphy, D., Ries, P., Romans, L., Sibois, A., Sibthorpe, A., Szilagyi, B., Vallisneri, M., and Willis, P.: GipsyX/RTGx, a new tool set for space geodetic operations and research, *Advances in Space Research*, 66, 469–489, <https://doi.org/10.1016/j.asr.2020.04.015>, 2020.
- Bevis, M. and Brown, A.: Trajectory models and reference frames for crustal motion geodesy, *Journal of Geodesy*, 88, 283–311, <https://doi.org/10.1007/s00190-013-0685-5>, 2014.
- 565 Boehm, J., Werl, B., and Schuh, H.: Troposphere mapping functions for GPS and very long baseline interferometry from European Centre for Medium-Range Weather Forecasts operational analysis data, *Journal of Geophysical Research: Solid Earth*, 111, 1–9, <https://doi.org/10.1029/2005JB003629>, 2006.
- Boulze, H., Fleitout, L., Klein, E., and Vigny, C.: Post-seismic motion after 3 Chilean megathrust earthquakes: a clue for a linear asthenospheric viscosity, *Geophysical Journal International*, 231, 1471–1478, 2022.
- 570



- Cifuentes, I. L.: The 1960 Chilean earthquakes, *Journal of Geophysical Research: Solid Earth*, 94, 665–680, 1989.
- Comte, D. and Pardo, M.: Reappraisal of great historical earthquakes in the northern Chile and southern Peru seismic gaps, *Natural Hazards*, 4, 23–44, 1991.
- Coreform Cubit: [Computer software]. Orem, UT: Coreform LLC., <http://coreform.com>, 2023.
- 575 Doin, M. P., Lasserre, C., Peltzer, G., Cavalié, O., and Doubre, C.: Corrections of stratified tropospheric delays in SAR interferometry: Validation with global atmospheric models, *Journal of Applied Geophysics*, 69, 35–50, <https://doi.org/10.1016/j.jappgeo.2009.03.010>, 2009.
- Doin, M.-P., Lodge, F., Guillaso, S., Jolivet, R., Lasserre, C., Ducret, G., Grandin, R., Pathier, E., and Pinel, V.: Presentation of the small baseline NSBAS processing chain on a case example: the Etna deformation monitoring from 2003 to 2010 using Envisat data, *Proceedings of the ESA 'Fringe 2011 Workshop'*, Frascati, Italy, (19–23 September 2011), 2011, 19–23, [http://www.geologie.ens.fr/~grandin/upload/Doin\\_2012\\_NSBAS.pdf%5Cnhttp://www.gps.caltech.edu/~jolivetr/jolivetr/Publications\\_files/Proceedings\\_of\\_the\\_Fringe\\_symposium\\_2011\\_Doin.pdf](http://www.geologie.ens.fr/~grandin/upload/Doin_2012_NSBAS.pdf%5Cnhttp://www.gps.caltech.edu/~jolivetr/jolivetr/Publications_files/Proceedings_of_the_Fringe_symposium_2011_Doin.pdf), 2011.
- 580 Duputel, Z., Jiang, J., Jolivet, R., Simons, M., Rivera, L., Ampuero, J.-P., Riel, B., Owen, S. E., Moore, A. W., Samsonov, S. V., Ortega-Culaciati, F., and Minson, S. E.: The Iquique earthquake sequence of April 2014: Bayesian modeling accounting for prediction uncertainty, *Geophysical Research Letters*, 42, 7949–7957, <https://doi.org/10.1002/2015GL065402>, 2015.
- Foster, James, Bevis, and Michael: Pisagua Megathrust Bolivia RAPID Response GPS Network, The GAGE Facility operated by EarthScope Consortium, *GPS/GNSS Observations (Aggregation of Multiple Datasets)*, <https://doi.org/10.7283/T5DJ5D0X>, 2014.
- Gao, Y., Tilmann, F., van Herwaarden, D. P., Thrastarson, S., Fichtner, A., Heit, B., Yuan, X., and Schurr, B.: Full Waveform Inversion Beneath the Central Andes: Insight Into the Dehydration of the Nazca Slab and Delamination of the Back-Arc Lithosphere, *Journal of Geophysical Research: Solid Earth*, 126, <https://doi.org/10.1029/2021JB021984>, 2021.
- 590 Giambiagi, L., Tassara, A., Echaurren, A., Julve, J., Quiroga, R., Barrionuevo, M., Liu, S., Echeverría, I., Mardónez, D., Suriano, J., Mescua, J., Lossada, A. C., Spagnotto, S., Bertoa, M., and Lothari, L.: Crustal anatomy and evolution of a subduction-related orogenic system: Insights from the Southern Central Andes (22–35°S), *Earth-Science Reviews*, 232, <https://doi.org/10.1016/j.earscirev.2022.104138>, 2022.
- Grandin, R.: Interferometric Processing of SLC Sentinel-1 TOPS Data, 2017.
- 595 Hayes, G. P., Moore, G. L., Portner, D. E., Hearne, M., Flamme, H., Furtney, M., and Smoczyk, G. M.: Zone Geometry Model, *Science*, 362, 58–61, 2018.
- Heidarzadeh, M., Murotani, S., Satake, K., Ishibe, T., and Gusman, A. R.: Source model of the 16 September 2015 Illapel, Chile, Mw 8.4 earthquake based on teleseismic and tsunami data, *Geophysical Research Letters*, 43, 643–650, <https://doi.org/10.1002/2015GL067297>, 2016.
- 600 Ho Tong Minh, D., Hanssen, R., Doin, M., and Pathier, E.: Advanced Methods for Timex2010;series InSAR, pp. 125–153, <https://doi.org/10.1002/9781119986843.ch5>, 2022.
- Hoffmann, F., Metzger, S., Moreno, M., Deng, Z., Sippl, C., Ortega-Culaciati, F., and Oncken, O.: Characterizing Afterslip and Ground Displacement Rate Increase Following the 2014 Iquique-Pisagua Mw 8.1 Earthquake, Northern Chile, *Journal of Geophysical Research: Solid Earth*, 123, 4171–4192, <https://doi.org/10.1002/2017JB014970>, 2018.
- 605 Hormazábal, J., Moreno, M., Ortega-Culaciati, F., Báez, J. C., Peña, C., Sippl, C., González-Vidal, D., Ruiz, J., Metzger, S., and Yoshioka, S.: Fast relocking and afterslip-seismicity evolution following the 2015 Mw 8.3 Illapel earthquake in Chile, *Scientific Reports*, 13, 19 511, 2023.



- Hu, Y., Wang, K., He, J., Klotz, J., and Khazaradze, G.: Three-dimensional viscoelastic finite element model for postseismic deformation of the great 1960 Chile earthquake, *Journal of Geophysical Research: Solid Earth*, 109, 2004.
- 610 Hu, Y., Bürgmann, R., Uchida, N., Banerjee, P., and Freymueller, J. T.: Stress-driven relaxation of heterogeneous upper mantle and time-dependent afterslip following the 2011 Tohoku earthquake, *Journal of Geophysical Research: Solid Earth*, 121, 385–411, 2016.
- Hu, Z., Hu, Y., and Bodunde, S. S.: Viscoelastic relaxation of the upper mantle and afterslip following the 2014 MW8.1 Iquique earthquake, *Earthquake Research Advances*, 1, 100 002, <https://doi.org/10.1016/J.EQREA.2021.100002>, 2021.
- Itoh, Y., Nishimura, T., Wang, K., and He, J.: New megathrust locking model for the southern kurile subduction zone incorporating viscoelastic relaxation and non-uniform compliance of upper plate, *Journal of Geophysical Research: Solid Earth*, 126, e2020JB019981, 2021.
- 615 Itoh, Y., Socquet, A., and Radiguet, M.: Largest aftershock nucleation driven by afterslip during the 2014 Iquique sequence, *Geophysical Research Letters*, 50, e2023GL104 852, 2023.
- Jara, J., Socquet, A., Marsan, D., and Bouchon, M.: Long-Term Interactions Between Intermediate Depth and Shallow Seismicity in North Chile Subduction Zone, *Geophysical Research Letters*, 44, 9283–9292, <https://doi.org/10.1002/2017GL075029>, 2017.
- 620 Jara, J., Sánchez-Reyes, H., Socquet, A., Cotton, F., Virieux, J., Maksymowicz, A., Díaz-Mojica, J., Walpersdorf, A., Ruiz, J., Cotte, N., and Norabuena, E.: Kinematic study of Iquique 2014 Mw 8.1 earthquake: Understanding the segmentation of the seismogenic zone, *Earth and Planetary Science Letters*, 503, 131–143, <https://doi.org/10.1016/j.epsl.2018.09.025>, 2018.
- Jolivet, R., Grandin, R., Lasserre, C., Doin, M. P., and Peltzer, G.: Systematic InSAR tropospheric phase delay corrections from global meteorological reanalysis data, *Geophysical Research Letters*, 38, 1–6, <https://doi.org/10.1029/2011GL048757>, 2011.
- 625 Jolivet, R., Simons, M., Duputel, Z., Olive, J. A., Bhat, H. S., and Bletery, Q.: Interseismic Loading of Subduction Megathrust Drives Long-Term Uplift in Northern Chile, *Geophysical Research Letters*, 47, 1–11, <https://doi.org/10.1029/2020>.
- Kanamori, H.: The Energy Release in Great Earthquakes, *Journal of Geophysical Research*, 82, 1977.
- Klein, E., Fleitout, L., Vigny, C., and Garaud, J. D.: Afterslip and viscoelastic relaxation model inferred from the large-scale postseismic deformation following the 2010 Mw 8.8 Maule earthquake (Chile), *Geophysical Journal International*, 205, 1455–1472, <https://doi.org/10.1093/gji/ggw086>, 2016.
- 630 Lemrabet, L., Doin, M. P., Lasserre, C., and Durand, P.: Referencing of Continental-Scale InSAR-Derived Velocity Fields: Case Study of the Eastern Tibetan Plateau, *Journal of Geophysical Research: Solid Earth*, 128, 1–28, <https://doi.org/10.1029/2022JB026251>, 2023.
- Li, S., Moreno, M., Bedford, J., Rosenau, M., Heidbach, O., Melnick, D., and Oncken, O.: Postseismic uplift of the Andes following the 2010 Maule earthquake: Implications for mantle rheology, *Geophysical Research Letters*, 44, 1768–1776, <https://doi.org/10.1002/2016GL071995>, 2017.
- 635 Li, S., Bedford, J., Moreno, M., Barnhart, W. D., Rosenau, M., and Oncken, O.: Spatiotemporal Variation of Mantle Viscosity and the Presence of Cratonic Mantle Inferred From 8 Years of Postseismic Deformation Following the 2010 Maule, Chile, Earthquake, *Geochemistry, Geophysics, Geosystems*, 19, 3272–3285, <https://doi.org/10.1029/2018GC007645>, 2018.
- 640 Li, S., Fukuda, J., and Oncken, O.: Geodetic Evidence of Time-Dependent Viscoelastic Interseismic Deformation Driven by Megathrust Locking in the Southwest Japan Subduction Zone, *Geophysical Research Letters*, 47, 1–10, <https://doi.org/10.1029/2019GL085551>, 2020.
- Lin, Y. N. N., Sladen, A., Ortega-Culaciati, F., Simons, M., Avouac, J. P., Fielding, E. J., Brooks, B. A., Bevis, M., Genrich, J., Rietbrock, A., Vigny, C., Smalley, R., and Socquet, A.: Coseismic and postseismic slip associated with the 2010 Maule Earthquake, Chile: Characterizing the Arauco Peninsula barrier effect, *Journal of Geophysical Research: Solid Earth*, 118, 3142–3159, <https://doi.org/10.1002/jgrb.50207>, 2013.
- 645



- López-Quiroz, P., Doin, M. P., Tupin, F., Briole, P., and Nicolas, J. M.: Time series analysis of Mexico City subsidence constrained by radar interferometry, *Journal of Applied Geophysics*, 69, 1–15, <https://doi.org/10.1016/j.jappgeo.2009.02.006>, 2009.
- Loverly, B., Chlieh, M., Norabuena, E., Villegas-Lanza, J., Radiguet, M., Cotte, N., Tsapong-Tsague, A., Quiroz, W., Sierra Farfán, C., Simons, M., et al.: Heterogeneous locking and earthquake potential on the South Peru megathrust from dense GNSS network, *Journal of Geophysical Research: Solid Earth*, 129, e2023JB027114, 2024.
- 650 Luo, H. and Wang, K.: Postseismic geodetic signature of cold forearc mantle in subduction zones, *Nature Geoscience*, 14, 104–109, <https://doi.org/10.1038/s41561-020-00679-9>, 2021a.
- Luo, H. and Wang, K.: Postseismic geodetic signature of cold forearc mantle in subduction zones, *Nature Geoscience*, 14, 104–109, 2021b.
- Luo, H. and Wang, K.: Finding simplicity in the complexity of postseismic coastal uplift and subsidence following great subduction earthquakes, *Journal of Geophysical Research: Solid Earth*, 127, e2022JB024471, 2022.
- 655 Lyard, F. H., Allain, D. J., Cancet, M., Carrère, L., and Picot, N.: FES2014 global ocean tide atlas: Design and performance, *Ocean Science*, 17, 615–649, <https://doi.org/10.5194/os-17-615-2021>, 2021.
- Marconato, L., Doin, M. P., Audin, L., and Pathier, E.: Ionospheric compensation in L-band InSAR time-series: Performance evaluation for slow deformation contexts in equatorial regions, *Science of Remote Sensing*, 9, <https://doi.org/10.1016/j.srs.2023.100113>, 2024.
- 660 Marill, L., Marsan, D., Socquet, A., Radiguet, M., Cotte, N., and Rousset, B.: Fourteen-Year Acceleration Along the Japan Trench, *Journal of Geophysical Research: Solid Earth*, 126, <https://doi.org/10.1029/2020JB021226>, 2021.
- Métois, M., Socquet, A., Vigny, C., Carrizo, D., Peyrat, S., Delorme, A., Maureira, E., Valderas-Bermejo, M.-C., and Ortega, I.: Revisiting the North Chile seismic gap segmentation using GPS-derived interseismic coupling, *Geophysical Journal International*, 194, 1283–1294, 2013.
- 665 Métois, M., Vigny, C., and Socquet, A.: Interseismic Coupling, Megathrust Earthquakes and Seismic Swarms Along the Chilean Subduction Zone (38°–18°S), *Pure and Applied Geophysics*, 173, 1431–1449, <https://doi.org/10.1007/s00024-016-1280-5>, 2016.
- Molina, D., Tassara, A., Abarca, R., Melnick, D., and Madella, A.: Frictional Segmentation of the Chilean Megathrust From a Multivariate Analysis of Geophysical, Geological, and Geodetic Data, *Journal of Geophysical Research: Solid Earth*, 126, <https://doi.org/10.1029/2020JB020647>, 2021.
- 670 Moreno, M., Rosenau, M., and Oncken, O.: 2010 Maule earthquake slip correlates with pre-seismic locking of Andean subduction zone, *Nature*, 467, 198–202, <https://doi.org/10.1038/nature09349>, 2010.
- Moreno, M., Melnick, D., Rosenau, M., Bolte, J., Klotz, J., Echtler, H., Baez, J., Bataille, K., Chen, J., Bevis, M., Hase, H., and Oncken, O.: Heterogeneous plate locking in the South-Central Chile subduction zone: Building up the next great earthquake, *Earth and Planetary Science Letters*, 305, 413–424, <https://doi.org/10.1016/j.epsl.2011.03.025>, 2011.
- 675 Muto, J., Moore, J., Barbot, S., Iinuma, T., Ohta, Y., and Iwamori, H.: Coupled afterslip and transient mantle flow after the 2011 Tohoku earthquake, *Science Advances*, 5, eaaw1164, 2019.
- Peyrat, S., Campos, J., de Chabaliér, J.-B., Perez, A., Bonvalot, S., Bouin, M.-P., Legrand, D., Nercessian, A., Charade, O., Patau, G., et al.: Tarapacá intermediate-depth earthquake (Mw 7.7, 2005, northern Chile): A slab-pull event with horizontal fault plane constrained from seismologic and geodetic observations, *Geophysical Research Letters*, 33, 2006.
- 680 Poli, P., Maksymowicz, A., and Ruiz, S.: The Mw 8.3 Illapel earthquake (Chile): Preseismic and postseismic activity associated with hydrated slab structures, *Geology*, 45, 247–250, 2017.
- Pollitz, F., Banerjee, P., Grijalva, K., Nagarajan, B., and Bürgmann, R.: Effect of 3-D viscoelastic structure on post-seismic relaxation from the 2004 M= 9.2 Sumatra earthquake, *Geophysical Journal International*, 173, 189–204, 2008.



- Pons, M., Sobolev, S. V., Liu, S., and Neuharth, D.: Hindered Trench Migration Due To Slab Steepening Controls the Formation of the  
685 Central Andes, *Journal of Geophysical Research: Solid Earth*, 127, 1–21, <https://doi.org/10.1029/2022JB025229>, 2022.
- Rosen, P. A., Hensley, S., Peltzer, G., and Simons, M.: Updated repeat orbit interferometry package released, *Eos*, 85, 47,  
<https://doi.org/10.1029/2004EO050004>, 2004.
- Rousset, B., Barbot, S., Avouac, J.-P., and Hsu, Y.-J.: Postseismic deformation following the 1999 Chi-Chi earthquake, Taiwan: Implication  
for lower-crust rheology, *Journal of Geophysical Research: Solid Earth*, 117, 2012.
- 690 Ruiz, S., Metois, M., Fuenzalida, A., Ruiz, J., Leyton, F., Grandin, R., Vigny, C., Madariaga, R., and Campos, J.: Intense foreshocks and a  
slow slip event preceded the 2014 Iquique Mw8.1 earthquake, *Science*, pp. 1165–1169, <https://doi.org/10.1126/science.1256074>, 2014.
- Ruiz, S., Moreno, M., Melnick, D., Del Campo, F., Poli, P., Báez, J. C., Leyton, F., and Madariaga, R.: Reawakening of large earthquakes in  
south central Chile: The 2016 Mw 7.6 Chiloé event, *Geophysical Research Letters*, 44, 6633–6640, 2017.
- Schurr, B., Asch, G., Hainzl, S., Bedford, J., Hoechner, A., Palo, M., Wang, R., Moreno, M., Bartsch, M., Zhang, Y., Oncken, O., Tilmann,  
695 F., Dahm, T., Victor, P., Barrientos, S., and Vilotte, J. P.: Gradual unlocking of plate boundary controlled initiation of the 2014 Iquique  
earthquake, *Nature*, 512, 299–302, <https://doi.org/10.1038/nature13681>, 2014.
- Shrivastava, M. N., González, G., Moreno, M., Chlieh, M., Salazar, P., Reddy, C., Báez, J. C., Yáñez, G., González, J., and de La Llera, J. C.:  
Coseismic slip and afterslip of the 2015 Mw 8.3 Illapel (Chile) earthquake determined from continuous GPS data, *Geophysical Research  
Letters*, 43, 10–710, 2016.
- 700 Shrivastava, M. N., González, G., Moreno, M., Soto, H., Schurr, B., Salazar, P., and Báez, J. C.: Earthquake segmentation in northern Chile  
correlates with curved plate geometry, *Scientific reports*, 9, 4403, 2019.
- Sobolev, S. V. and Babeyko, A. Y.: What drives orogeny in the Andes?, *Geology*, 33, 617–620, <https://doi.org/10.1130/G21557.1>, 2005.
- Socquet, A., Valdes, J. P., Jara, J., Cotton, F., Walpersdorf, A., Cotte, N., Specht, S., Ortega-Culaciati, F., Carrizo, D., and Norabuena, E.:  
An 8 month slow slip event triggers progressive nucleation of the 2014 Chile megathrust, *Geophysical Research Letters*, 44, 4046–4053,  
705 <https://doi.org/10.1002/2017GL073023>, 2017.
- Socquet, A., Tsapong-Tsague, A., Lavery, B., Janex, G., and Radiguet, M.: Metadata and GNSS daily position solutions for permanent GNSS  
stations in South America., [https://doi.org/10.17178/GNSS.products.SouthAmerica\\_GIPSYX.daily](https://doi.org/10.17178/GNSS.products.SouthAmerica_GIPSYX.daily), 2023.
- Springer, M.: Interpretation of heat-flow density in the Central Andes, *Tectonophysics*, 306, 377–395, [https://doi.org/10.1016/S0040-1951\(99\)00067-0](https://doi.org/10.1016/S0040-1951(99)00067-0), 1999.
- 710 Suito, H. and Freymueller, J. T.: A viscoelastic and afterslip postseismic deformation model for the 1964 Alaska earthquake, *Journal of  
Geophysical Research: Solid Earth*, 114, 2009.
- Sun, T., Wang, K., Iinuma, T., Hino, R., He, J., Fujimoto, H., Kido, M., Osada, Y., Miura, S., Ohta, Y., et al.: Prevalence of viscoelastic  
relaxation after the 2011 Tohoku-oki earthquake, *Nature*, 514, 84–87, 2014.
- Tassara, A. and Echaurren, A.: Anatomy of the Andean subduction zone: Three-dimensional density model upgraded and compared against  
715 global-scale models, *Geophysical Journal International*, 189, 161–168, <https://doi.org/10.1111/j.1365-246X.2012.05397.x>, 2012.
- Tassara, A., Götze, H. J., Schmidt, S., and Hackney, R.: Three-dimensional density model of the Nazca plate and the Andean continental  
margin, *Journal of Geophysical Research: Solid Earth*, 111, 1–26, <https://doi.org/10.1029/2005JB003976>, 2006.
- Thollard, F., Clesse, D., Doin, M.-p., Donadieu, J., Durand, P., Grandin, R., Lasserre, C., Laurent, C., Deschamps-ostanciaux, E., Pathier, E.,  
Thollard, F., Clesse, D., Doin, M.-p., Donadieu, J., Durand, P., Thollard, F., Clesse, D., Doin, M.-p., Donadieu, J., Durand, P., Grandin,  
720 R., Lasserre, C., Laurent, C., and Deschamps-ostanciaux, E.: FLATSIM : The ForM @ Ter LArge-Scale Multi-Temporal Sentinel-I



- Interferometry Service To cite this version : HAL Id : hal-03397350 FLATSIM : the ForM @ Ter LArge-scale multi-Temporal Sentinel-1 Interferometry service, 2021.
- Tilmann, F., Zhang, Y., Moreno, M., Saul, J., Eckelmann, F., Palo, M., Deng, Z., Babeyko, A., Chen, K., Baez, J. C., Schurr, B., Wang, R., and Dahm, T.: The 2015 Illapel earthquake, central Chile: A type case for a characteristic earthquake?, *Geophysical Research Letters*, 43, 574–583, <https://doi.org/10.1002/2015GL066963>, 2016.
- Tissandier, R., Nocquet, J.-M., Klein, E., Vigny, C., Ojeda, J., and Ruiz, S.: Afterslip of the Mw 8.3 2015 Illapel Earthquake Imaged Through a Time-Dependent Inversion of Continuous and Survey GNSS Data, *Journal of Geophysical Research: Solid Earth*, 128, e2022JB024778, 2023.
- Tozer, B., Sandwell, D. T., Smith, W. H., Olson, C., Beale, J. R., and Wessel, P.: Global Bathymetry and Topography at 15 Arc Sec: SRTM15+, *Earth and Space Science*, 6, 1847–1864, <https://doi.org/10.1029/2019EA000658>, 2019.
- Twardzik, C., Vergnolle, M., Sladen, A., and Tsang, L. L.: Very early identification of a bimodal frictional behavior during the post-seismic phase of the 2015 Mw 8.3 Illapel, Chile, earthquake, *Solid Earth*, 12, 2523–2537, 2021.
- Vigny, C. and Klein, E.: The 1877 megathrust earthquake of North Chile two times smaller than thought? A review of ancient articles, *Journal of South American Earth Sciences*, 117, <https://doi.org/10.1016/j.jsames.2022.103878>, 2022.
- Wada, I. and Wang, K.: Common depth of slab-mantle decoupling: Reconciling diversity and uniformity of subduction zones, *Geochemistry, Geophysics, Geosystems*, 10, <https://doi.org/10.1029/2009GC002570>, 2009.
- Wada, I., Wang, K., He, J., and Hyndman, R. D.: Weakening of the subduction interface and its effects on surface heat flow, slab dehydration, and mantle wedge serpentinization, *Journal of Geophysical Research: Solid Earth*, 113, 1–15, <https://doi.org/10.1029/2007JB005190>, 2008.
- Wang, K.: Elastic and viscoelastic models of crustal deformation in subduction earthquake cycles, in: *The seismogenic zone of subduction thrust faults*, pp. 540–575, Columbia University Press, 2007.
- Wang, K., Hu, Y., and He, J.: Deformation cycles of subduction earthquakes in a viscoelastic Earth, *Nature*, 484, 327–332, 2012.
- Wang, M., Shen, Z. K., Wang, Y. Z., Bürgmann, R., Wang, F., Zhang, P. Z., Liao, H., Zhang, R., Wang, Q., Jiang, Z. S., Chen, W. T., Hao, M., Li, Y., Gu, T., Tao, W., Wang, K., and Xue, L.: Postseismic Deformation of the 2008 Wenchuan Earthquake Illuminates Lithospheric Rheological Structure and Dynamics of Eastern Tibet, *Journal of Geophysical Research: Solid Earth*, 126, 1–18, <https://doi.org/10.1029/2021JB022399>, 2021.
- Yuan, X., Sobolev, S. V., Kind, R., Oncken, O., Bock, G., Asch, G., Schurr, B., Graeber, F., Rudloff, A., Hanka, W., Wylegalla, K., Tibi, R., Haberland, C., Rietbrock, A., Giese, P., Wigger, P., Röwer, P., Zandt, G., Beck, S., Wallace, T., Pardo, M., and Comte, D.: Subduction and collision processes in the Central Andes constrained by converted seismic phases, *Nature*, 408, 958–961, <https://doi.org/10.1038/35050073>, 2000.

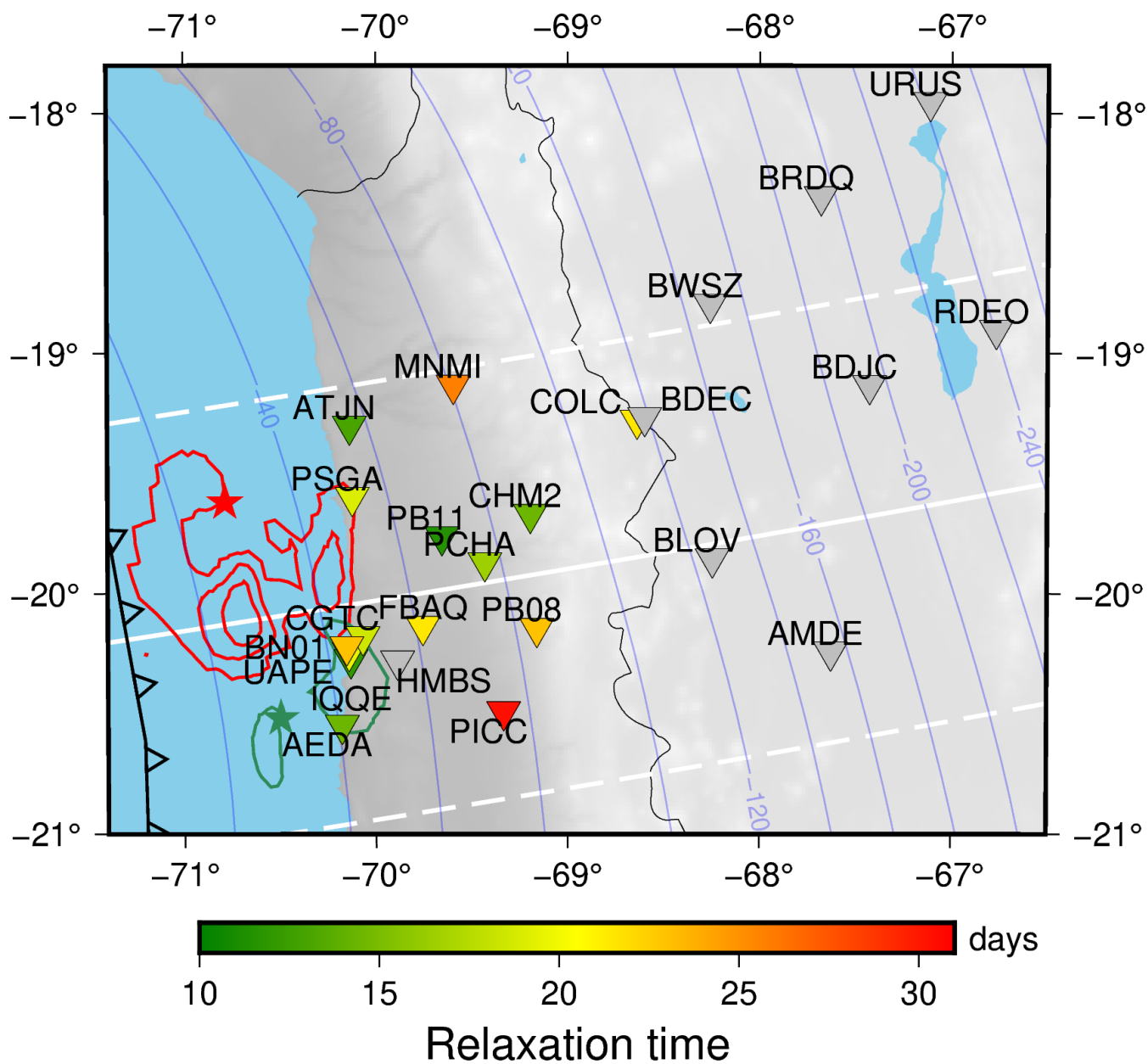
## Appendix A: Relaxation times and trajectory models

Figure A1 shows the relaxation time estimated at each station. Figures A2 to A26 show the trajectory model estimated for each station and its fit to the position time series. The stations are ordered by distance to the trench.



755 Eight stations have not enough data to constrain the interseismic and we use the interseismic from Jolivet et al. (2020) instead of the one inverted from the data. Ordered by distance to the trench, these stations are: PB11, BDEC, BWSZ, BLOV, BRDQ, AMDE, BDJC, RDEO.

Figure A27 shows an example of grid search exploration for estimating the amplitude and the relaxation time. Figure A28 shows the agreement between InSAR and GNSS.



**Figure A1.** Map of the studied area presented the location and the name of the GNSS stations. Triangles are color-coded by the relaxation time. The grey colour stands for stations which does not have enough early data to constrain the relaxation time.

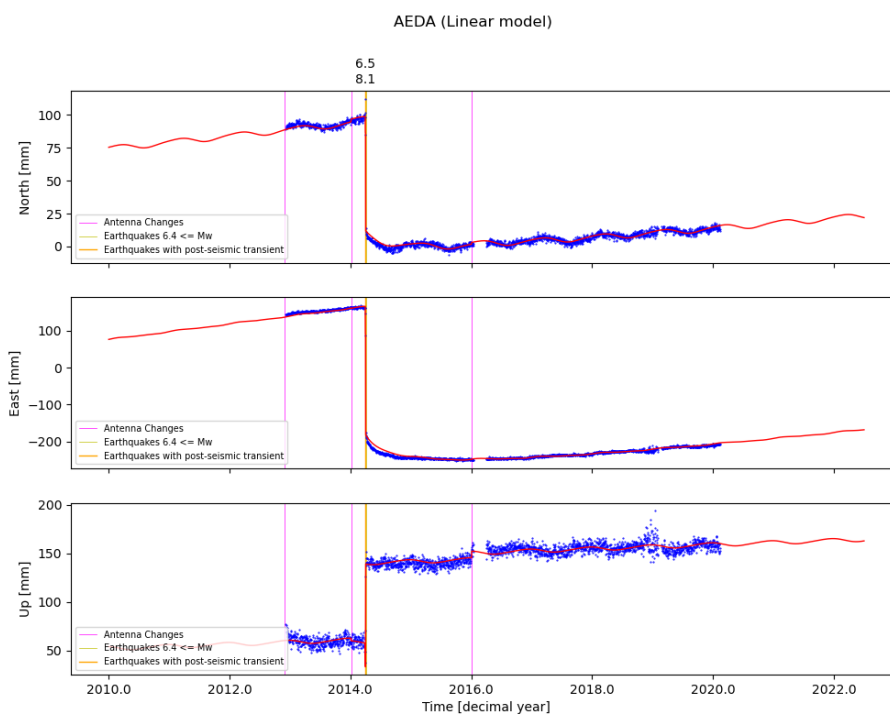


**Figure A2.** Trajectory model for the station AEDA. The three subplots present the three component of the displacement against the time. The blue dots present the data and the red curve the trajectory model inverted for each component. Pink lines present the dates of antenna changes. Yellow lines co-seismic jumps for earthquakes without modeled post-seismic and the orange line present the date of the co-seismic jump of the Iquique earthquake for which the post-seismic relaxation is modeled.

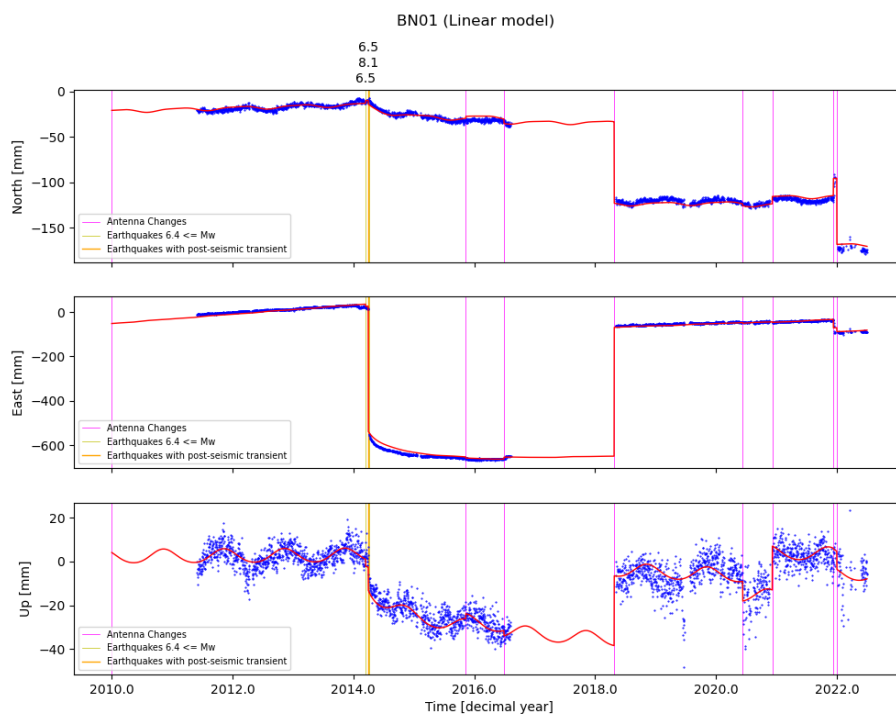


**Figure A3.** Trajectory model for the station BN01.

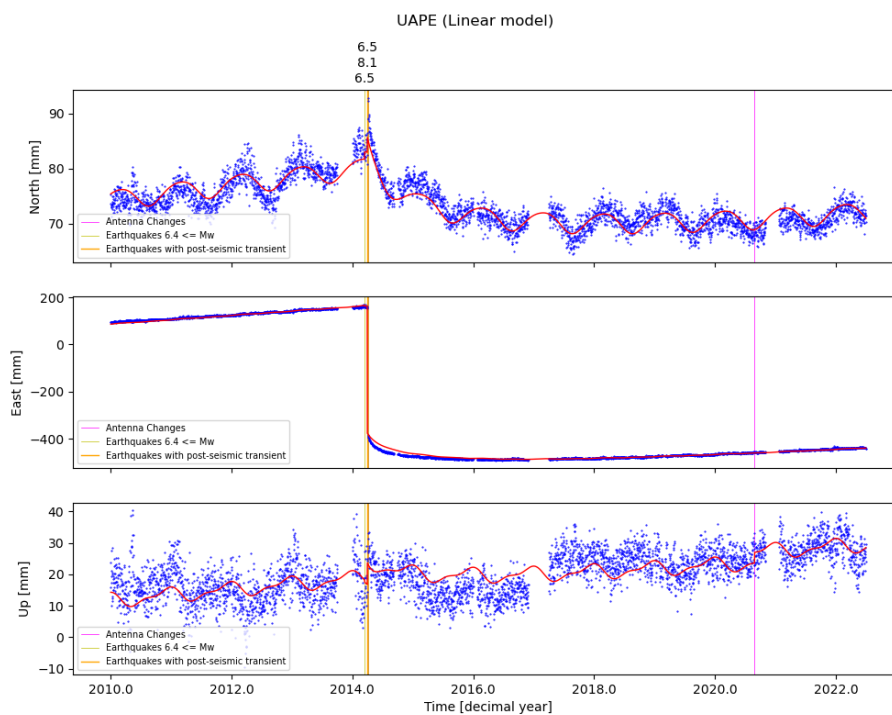


**Figure A4.** Trajectory model for the station UAPE.

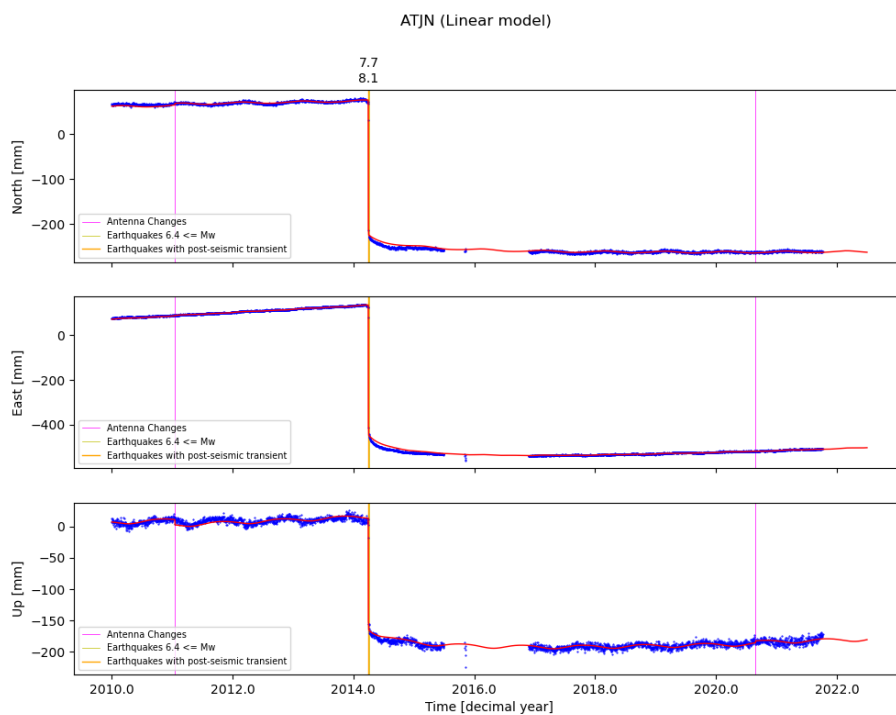


**Figure A5.** Trajectory model for the station ATJN.

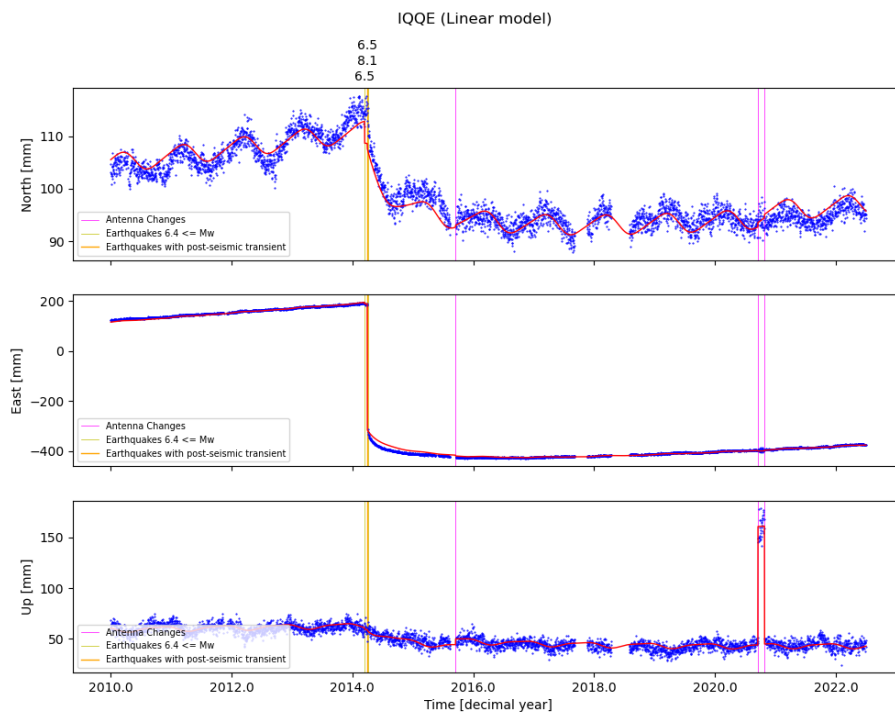


**Figure A6.** Trajectory model for the station IQQE.

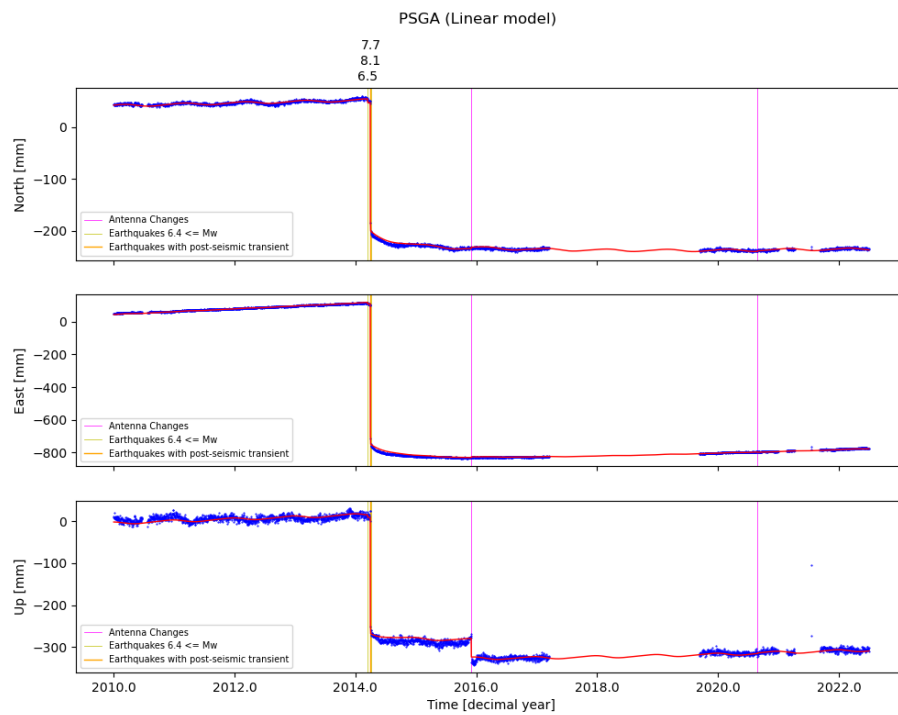


**Figure A7.** Trajectory model for the station PSGA.

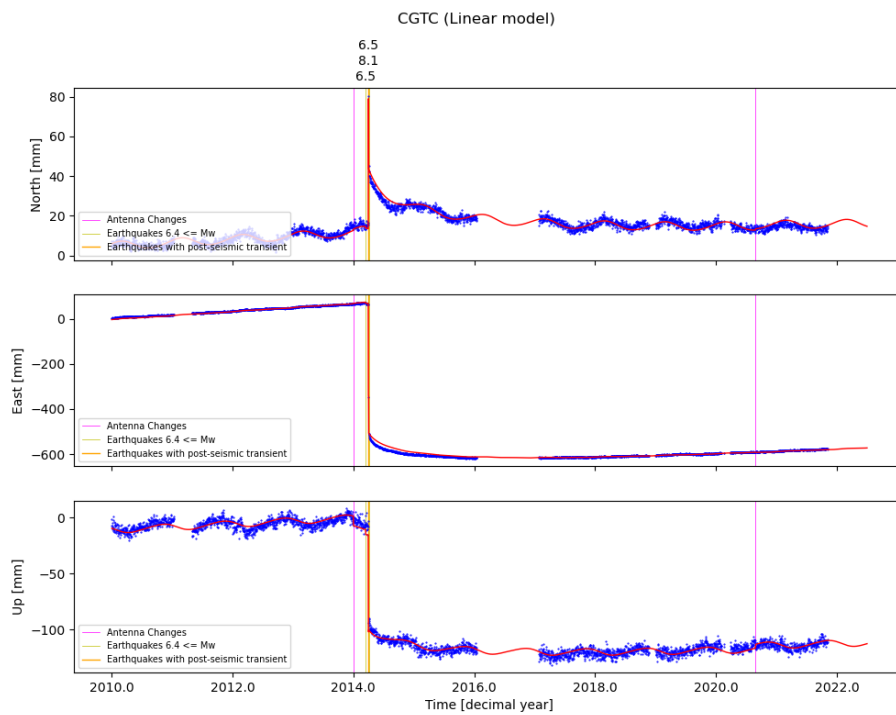


**Figure A8.** Trajectory model for the station CGTC.

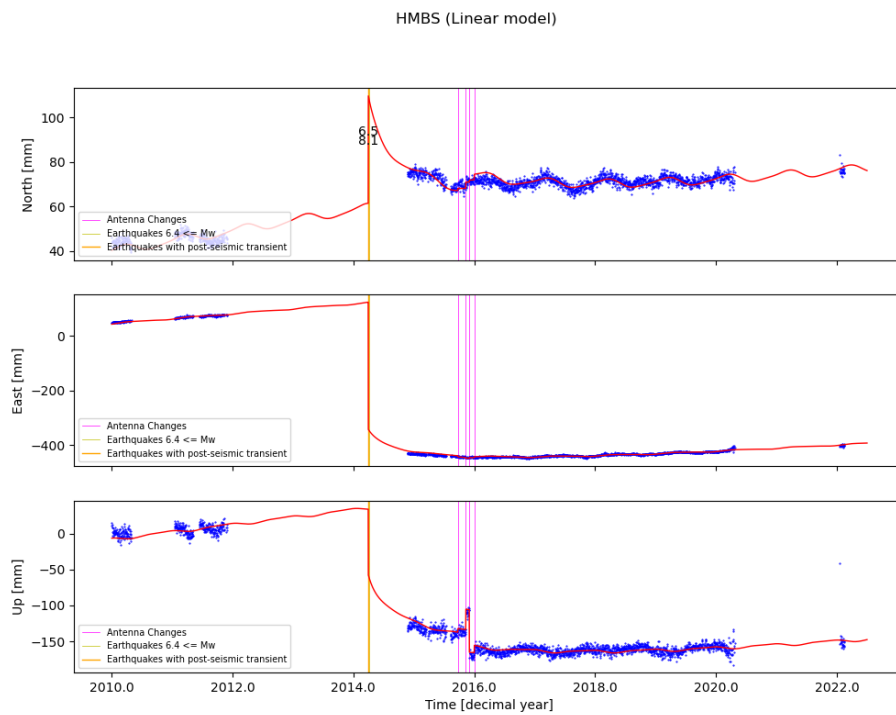


**Figure A9.** Trajectory model for the station HMBS.

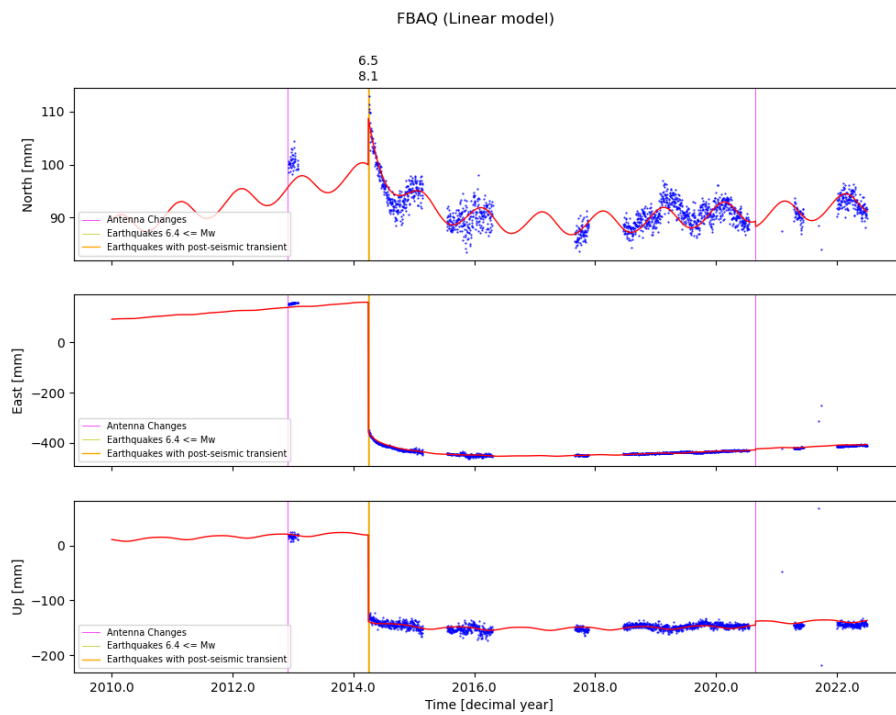


**Figure A10.** Trajectory model for the station FBAQ.

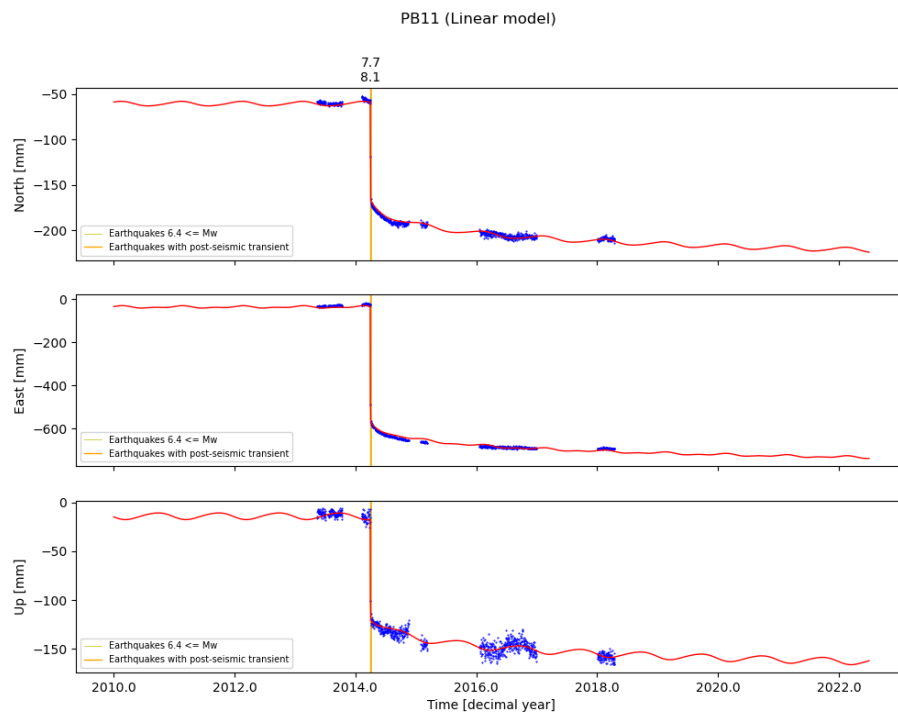


**Figure A11.** Trajectory model for the station PB11.

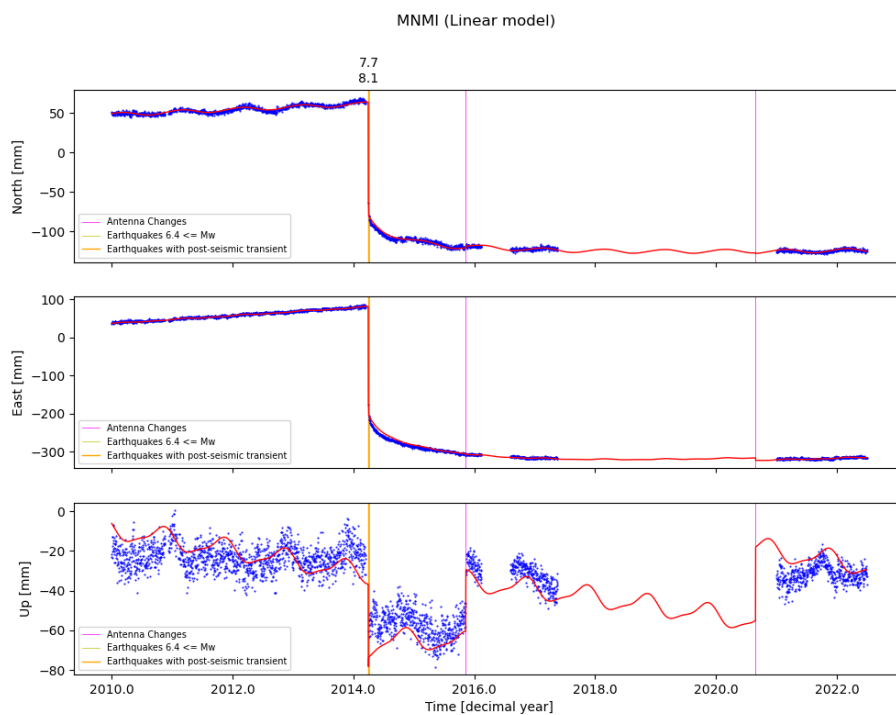


**Figure A12.** Trajectory model for the station MNMI.

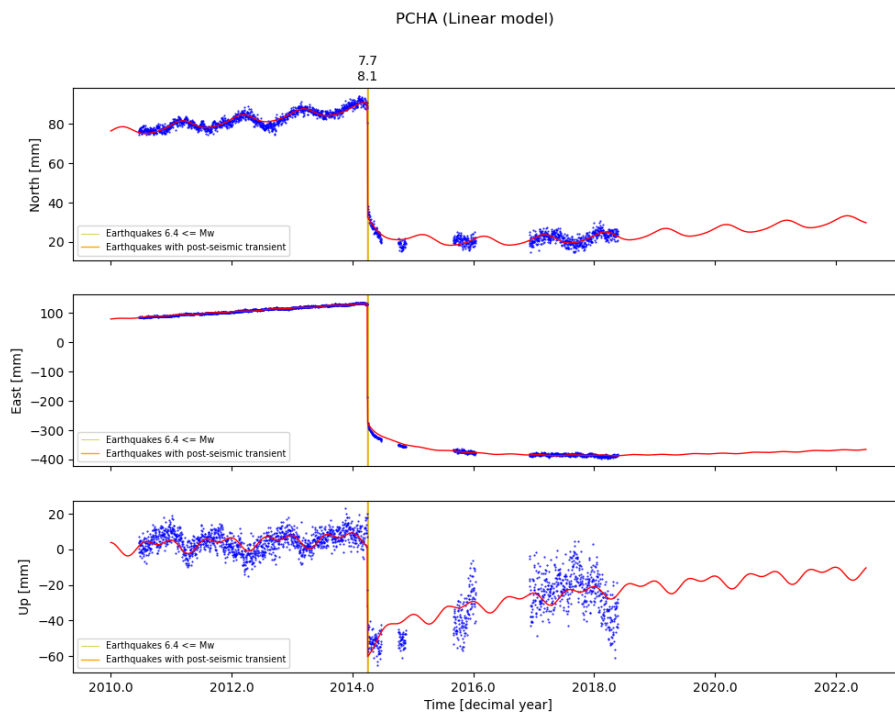


**Figure A13.** Trajectory model for the station PCHA.

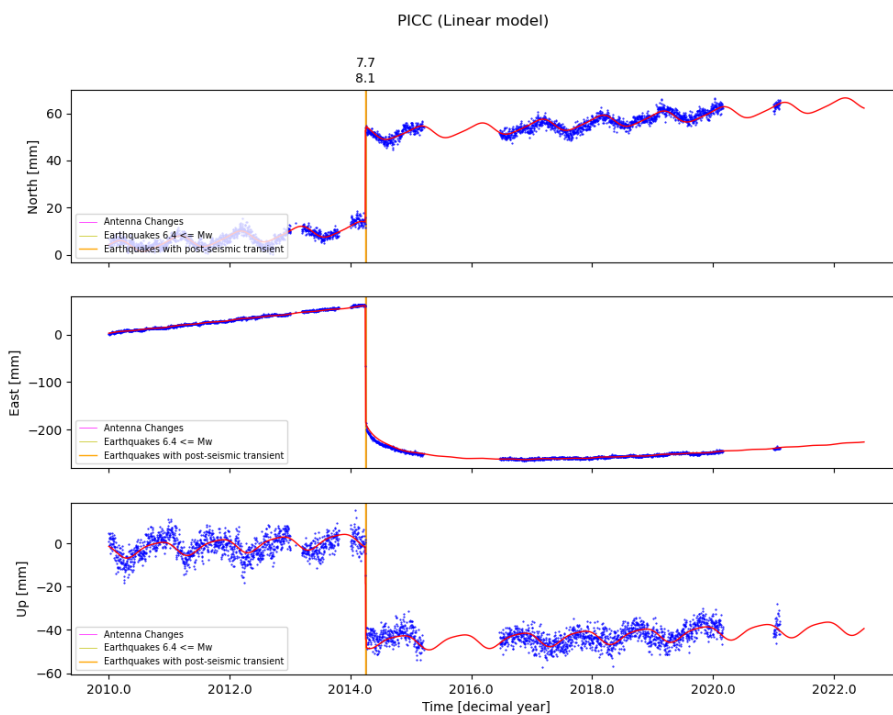


**Figure A14.** Trajectory model for the station PICC.

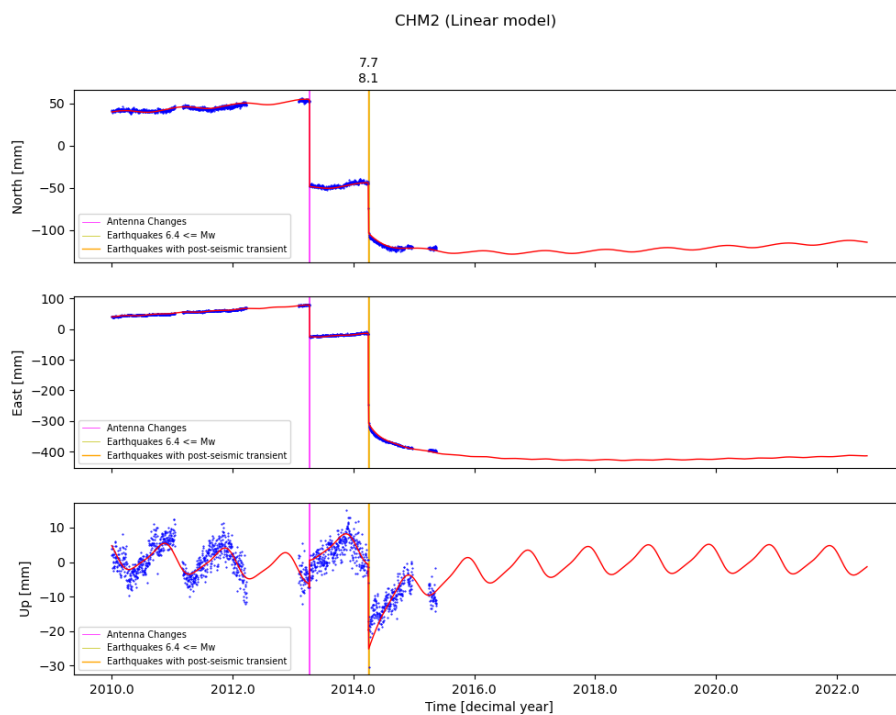


**Figure A15.** Trajectory model for the station CHM2.

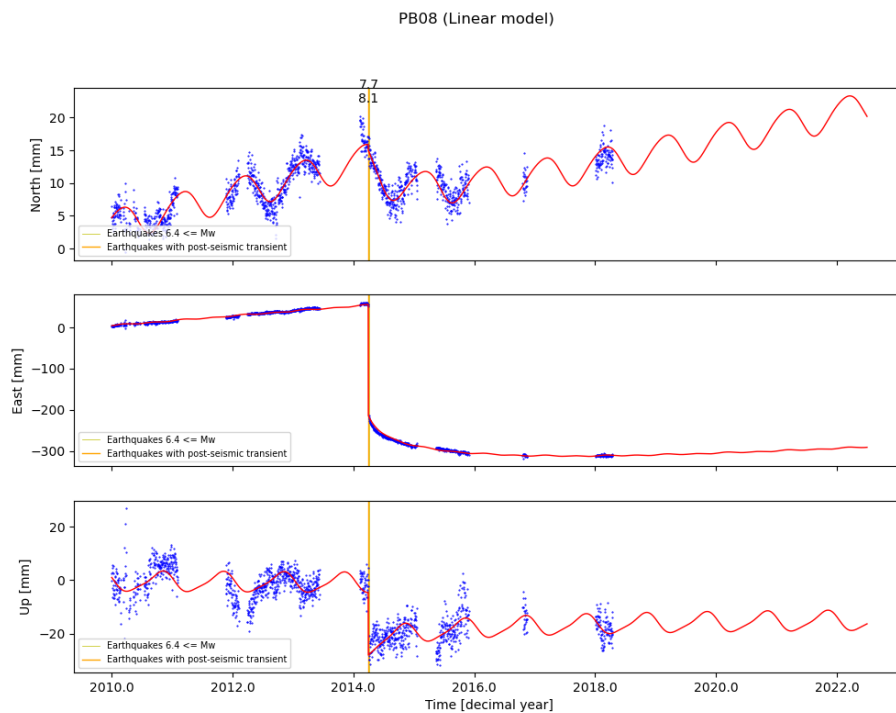


**Figure A16.** Trajectory model for the station PB08.

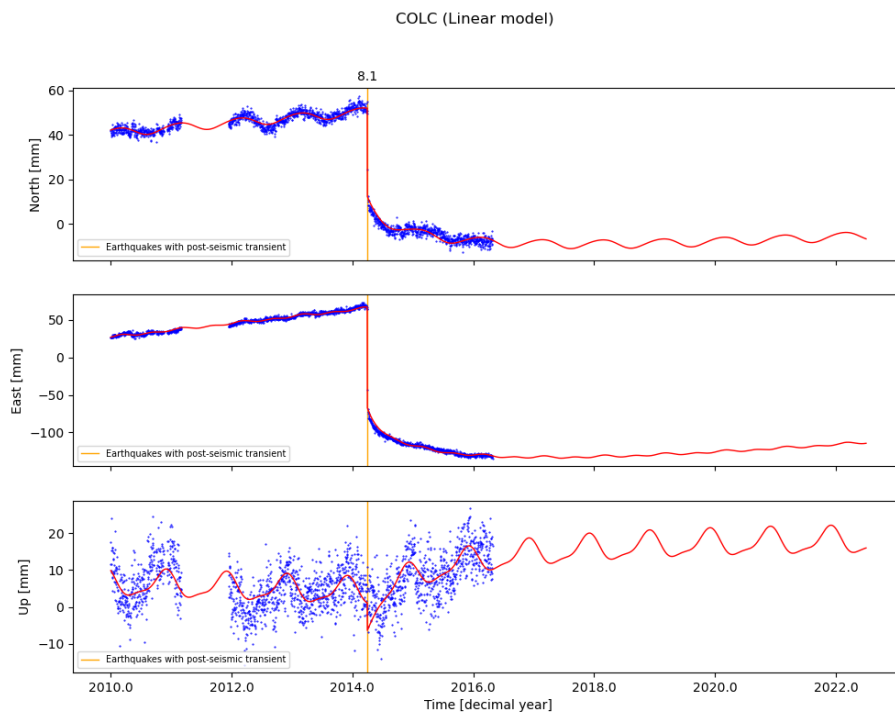


**Figure A17.** Trajectory model for the station COLC.

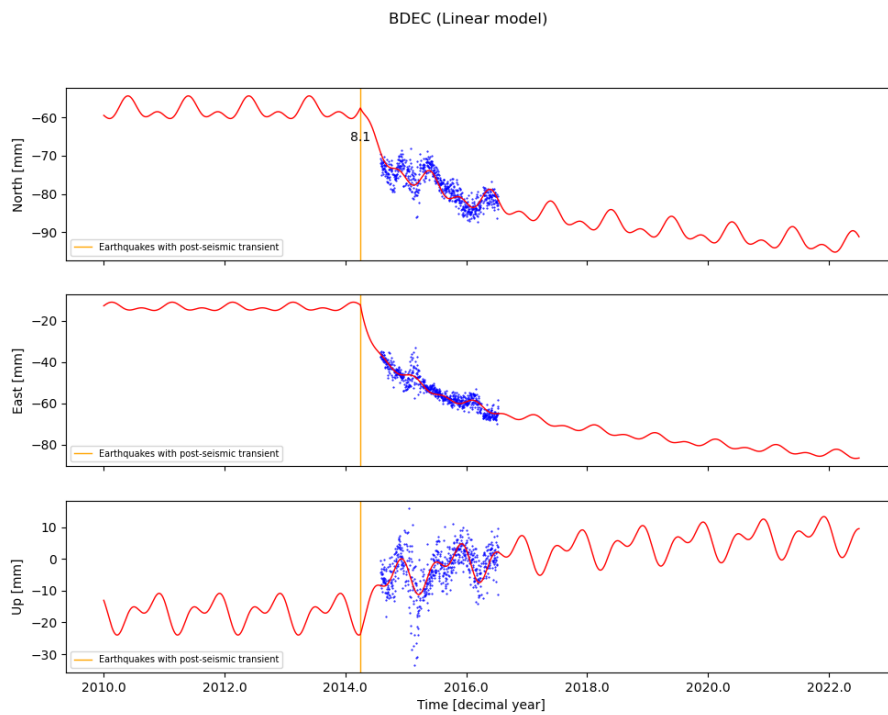


**Figure A18.** Trajectory model for the station BDEC.

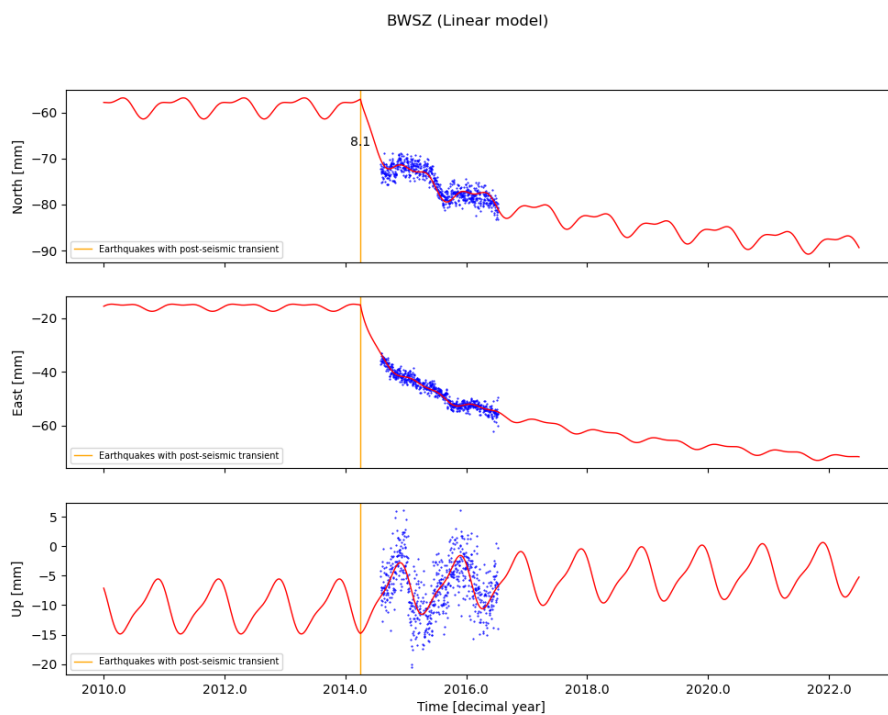


**Figure A19.** Trajectory model for the station BWSZ.

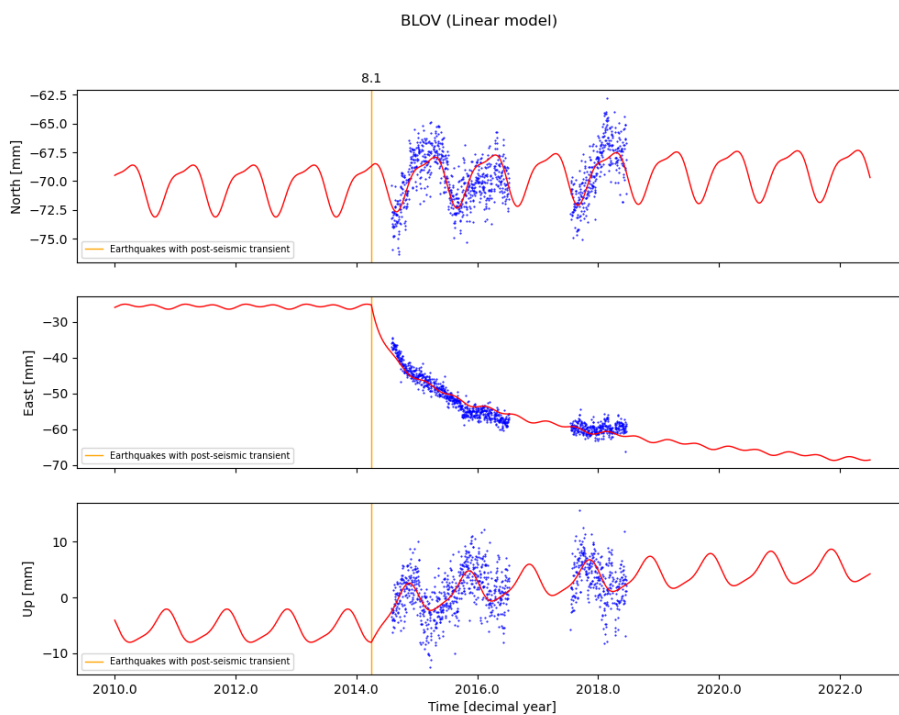


**Figure A20.** Trajectory model for the station BLOV.

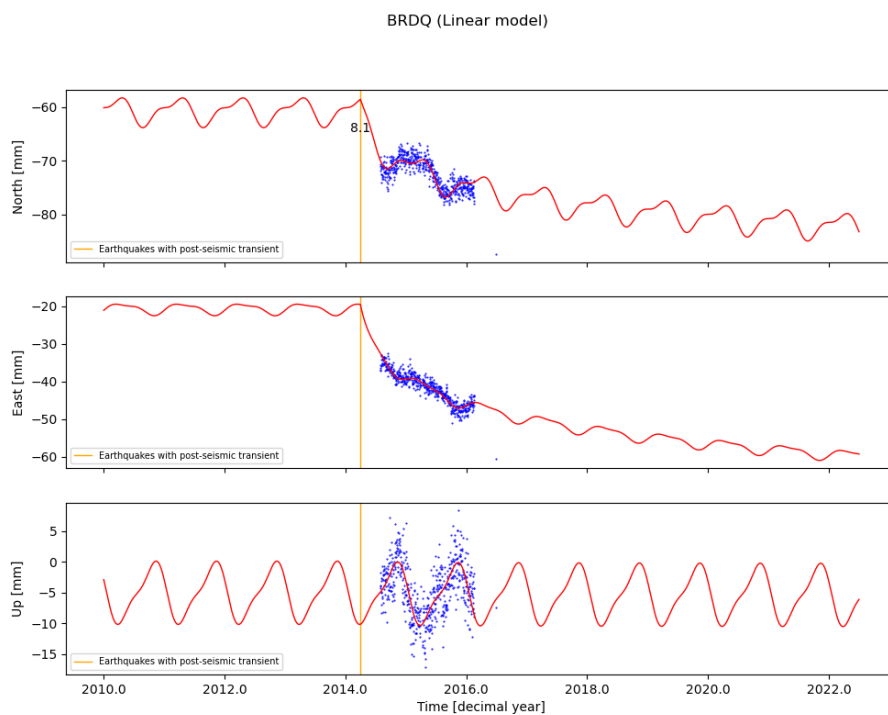


**Figure A21.** Trajectory model for the station BRDQ.

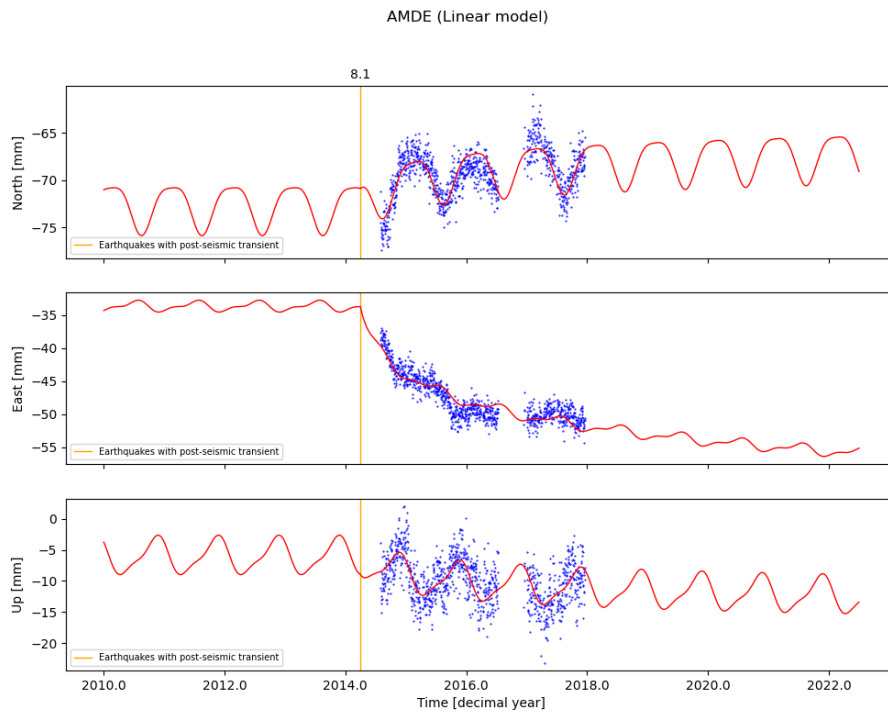


**Figure A22.** Trajectory model for the station AMDE.

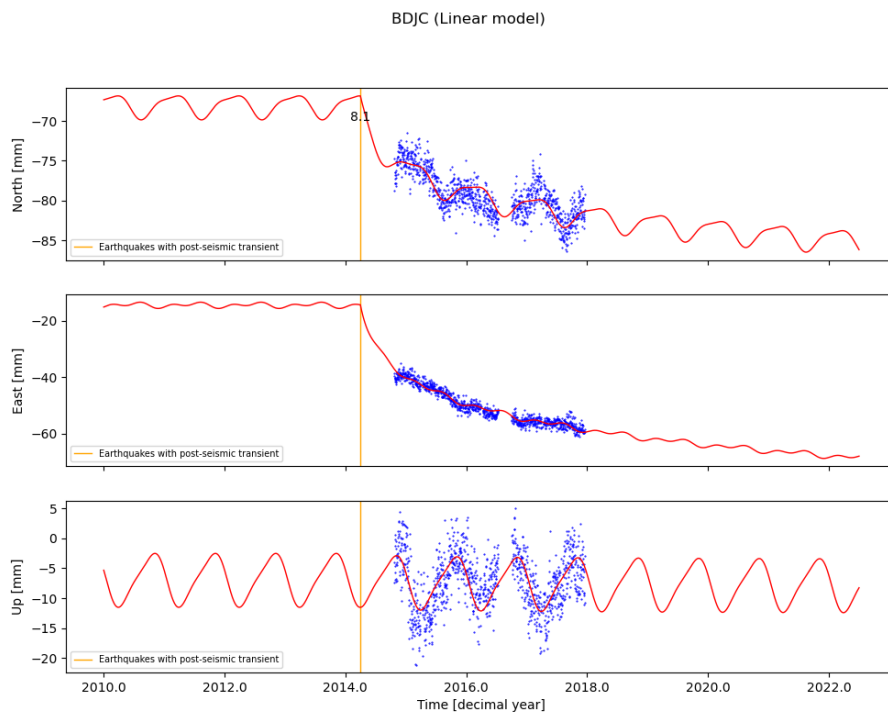


**Figure A23.** Trajectory model for the station BDJC.

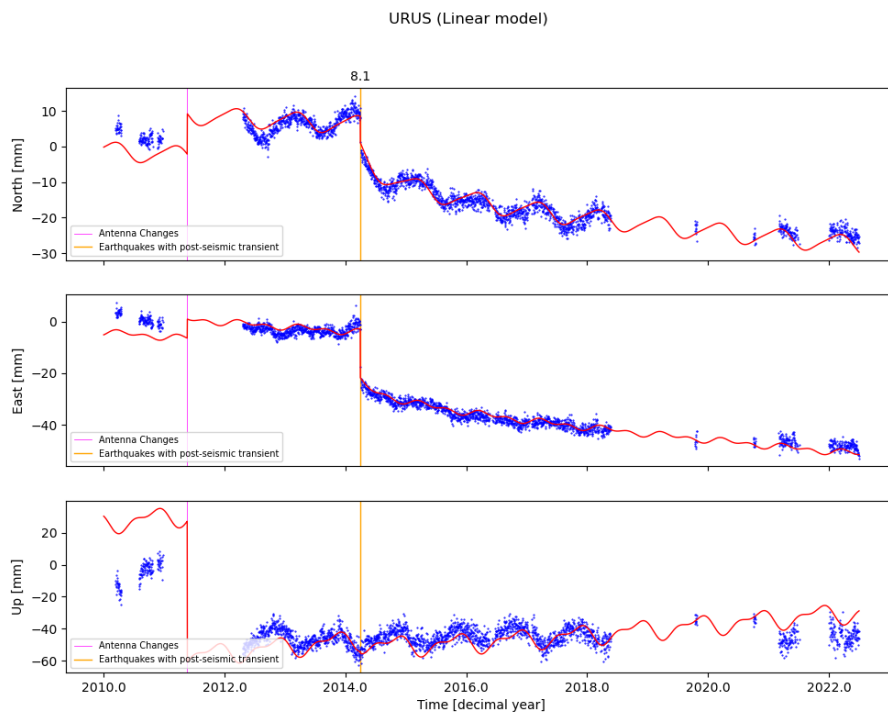


**Figure A24.** Trajectory model for the station URUS.

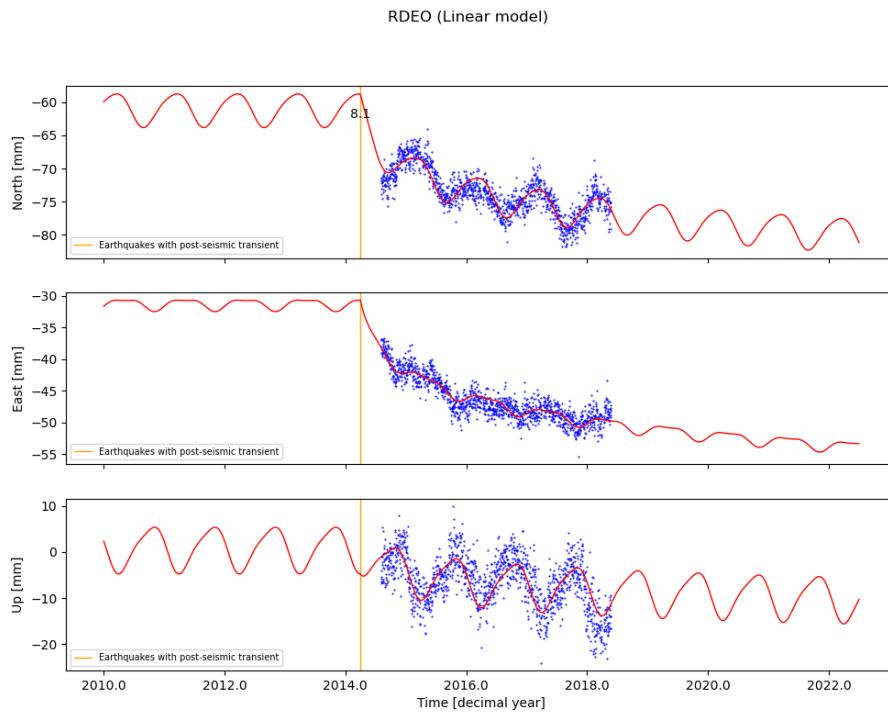


**Figure A25.** Trajectory model for the station RDEO.

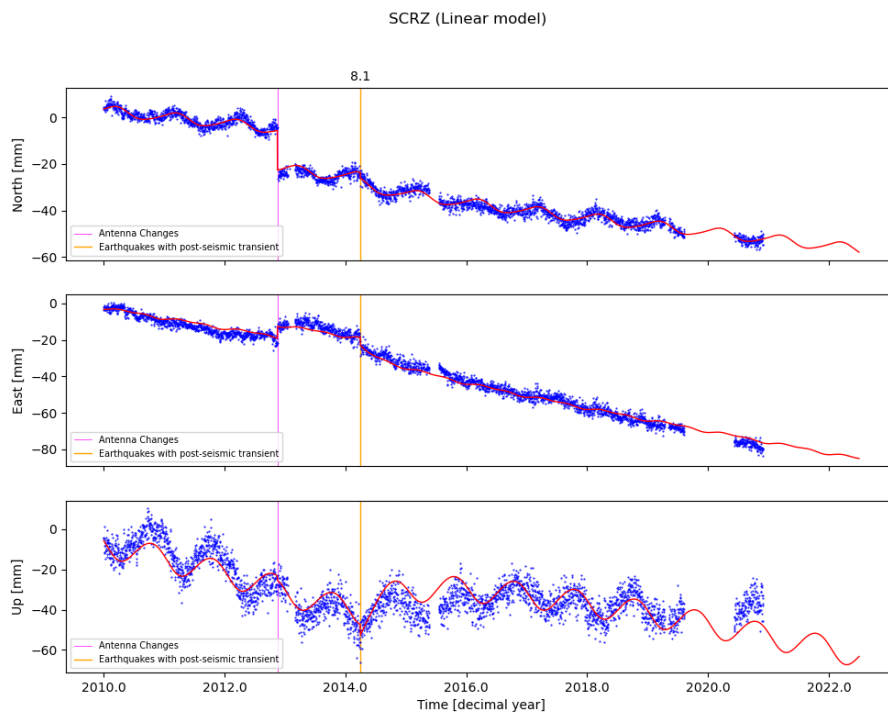


**Figure A26.** Trajectory model for the station SCRZ.



### MNMI East log\_L2

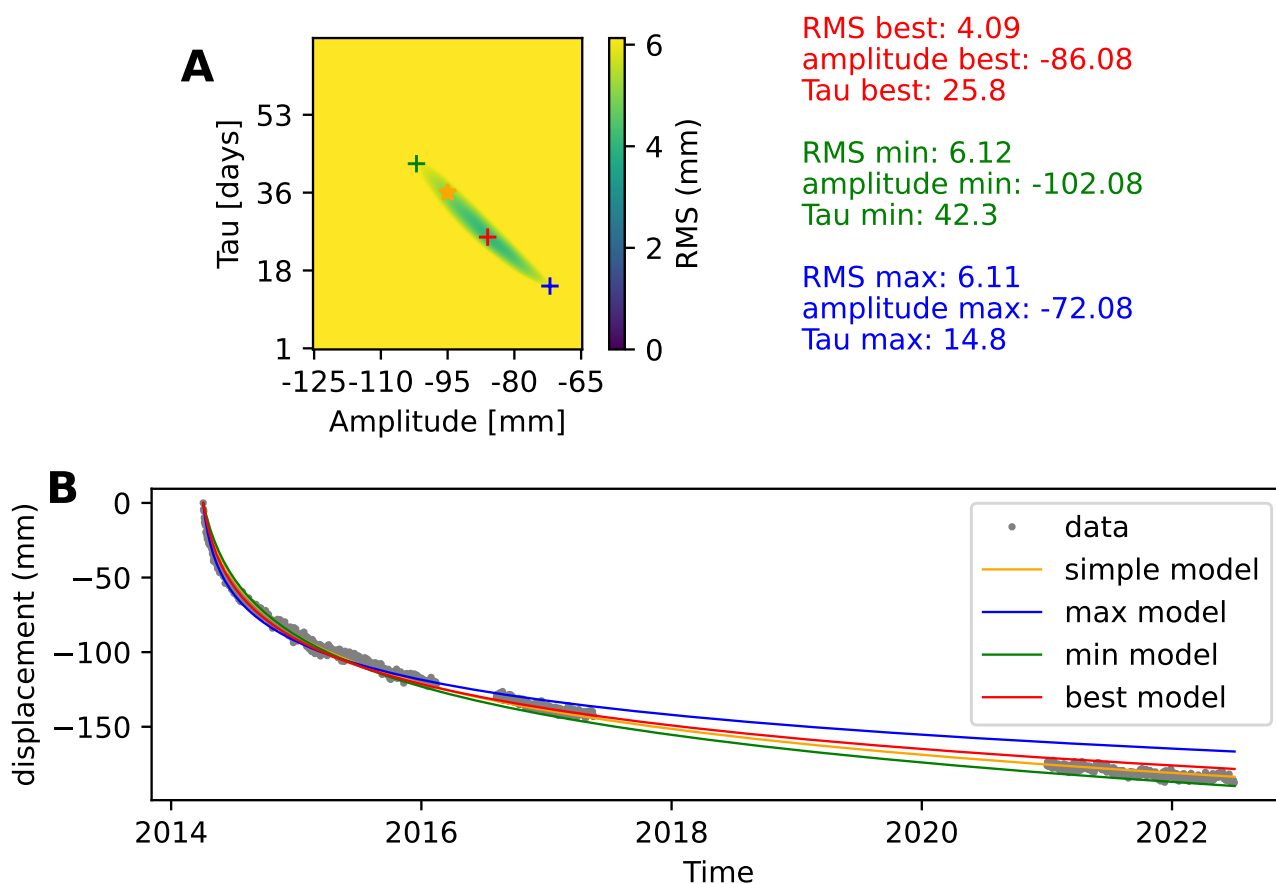


**Figure A27.** Example of a grid search of the exploration of the accepted values for the amplitude and the relaxation time (Tau) for the East component of the station MNMI. (A) Grid search for the fit of the times series between the amplitude and the relaxation time. The color shows the misfit computed with the L2 norm with the time as a logarithmic scale. The red cross is the best model found. The green and blue ones represent respectively the models with the minimum and maximum amplitude inside  $3 \times RMS_{best\_model}$ . The orange star corresponds to the simple model inverted with the time in a non-logarithmic scale. (B) Time series of the data represented with grey points and the different models which correspond to the ones described in the subfigure A.

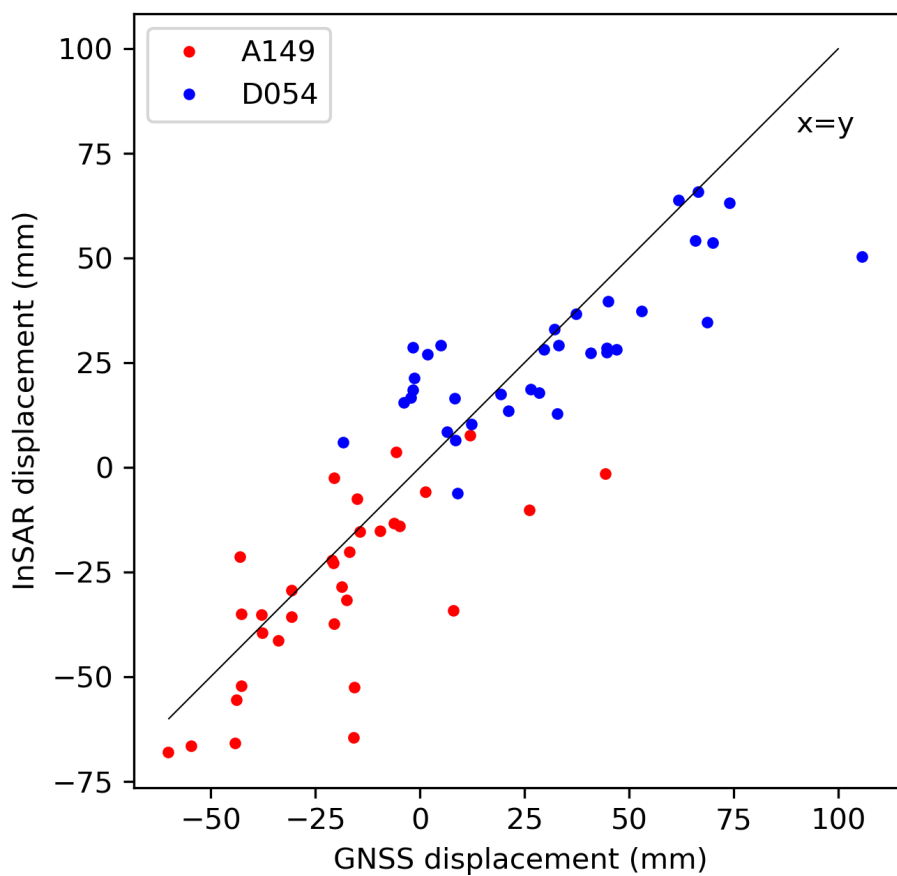


**Figure A28.** Comparison of the post-seismic displacement amplitudes measured from GNSS and InSAR. GNSS displacements are projected in the Line Of Sight (LOS). The InSAR data are extracted from the displacement map. Points on the line  $x=y$  indicate that the amplitude measured from GNSS and InSAR are the same. Red and blue points are the LOS displacements of track A149 and D054, respectively.



Station	Relaxation time (days)
AEDA	14.5
BN01	23.0
UAPE	19.5
ATJN	13.0
IQQE	12.0
PSGA	19.0
CGTC	18.5
HMBS	same as CGTC
FBAQ	21.5
PB11	11.5
MNMI	25.8
PCHA	16.5
PICC	30.4
CHM2	14.5
PB08	23.0
COLC	21.5
BDEC, BWSZ, BLOV, BRDQ, AMDE, BDJC, URUS, RDEO, SCRZ	same as COLC

**Table A1.** Relaxation times for the selected stations



## Appendix B: Further details on the modeling

### 760 B1 Python's code to transpose from Burgers formulation to generalized Maxwell

```
def Burgers4PyLith(shear_modulus_Kelvin, viscosity_Kelvin, shear_modulus_Maxwell,
viscosity_Maxwell):
    # calculate the four parameters p_1, p_2, q_1 and q_2
    p_1 = viscosity_Maxwell/shear_modulus_Maxwell
    + viscosity_Maxwell/shear_modulus_Kelvin + viscosity_Kelvin/shear_modulus_Kelvin
    p_2 = viscosity_Maxwell/shear_modulus_Maxwell
    * viscosity_Kelvin/shear_modulus_Kelvin
    q_1 = viscosity_Maxwell
    q_2 = viscosity_Maxwell*viscosity_Kelvin/shear_modulus_Kelvin
    # calculate the constant A
    A = np.sqrt(p_1**(2)-4*p_2) #
    # calculate hat_mu_1 and hat_mu_2
    hat_mu_1 = (q_1-q_2*(p_1-A)/(2*p_2))/A
    hat_mu_2 = (q_2*(p_1+A)/(2*p_2)-q_1)/A
    # calculate the relaxation times tau
    tau_1 = (2*p_2)/(p_1-A)
    tau_2 = (2*p_2)/(p_1+A)
    # calculate the total shear modulus
    total_shear_modulus = hat_mu_1+hat_mu_2
    # calculate the shear modulus
    mu_1 = hat_mu_1/total_shear_modulus
    mu_2 = hat_mu_2/total_shear_modulus
    # calculate the viscosities
    viscosity1 = hat_mu_1 * tau_1
    viscosity2 = hat_mu_2 * tau_2
    return(mu_1, viscosity1, mu_2, viscosity2, total_shear_modulus)
```

### B2 Results of the afterslip exploration

Here, we discuss the location and amplitude of the afterslip patch in our 2D model.

We vary the depth of the afterslip patch, which also changes its distance to the trench (Figure B2). Varying the depth mostly induces a horizontal offset of the model curve, the strongest constraint here being the fit to the vertical displacements at the



coastal stations (Figure B2 B and D). Our optimal model is selected with an afterslip mean depth of 36 km (i.e. 90 km from the Trench).

795 The width of the afterslip pulse (Figure B3) as well as the maximum slip value ( Figure B4) control the amplitude of the afterslip surface displacement. We perform a grid search over amplitude  $A_a$  and width  $A_w$  (see Figure B1) to assess the best fit to the coastal stations and find  $A_w = 24$  km and  $A_a = 0.4$  m. These values predict the minimum horizontal misfit for all stations in Figures B3 and B4.

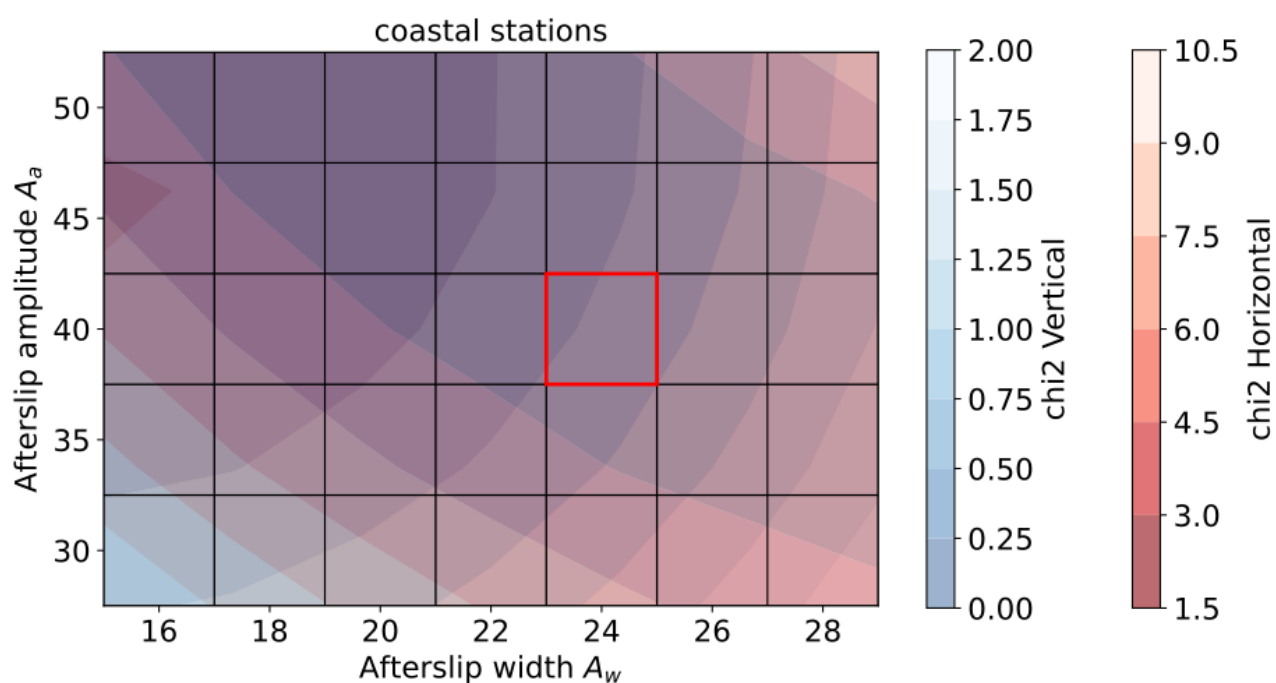


**Figure B1.** Grid search between afterslip amplitude  $A_a$  and the afterslip width  $A_w$  for the coastal stations where these parameters have the most influence. The preferred model parameters are highlighted by a red square.

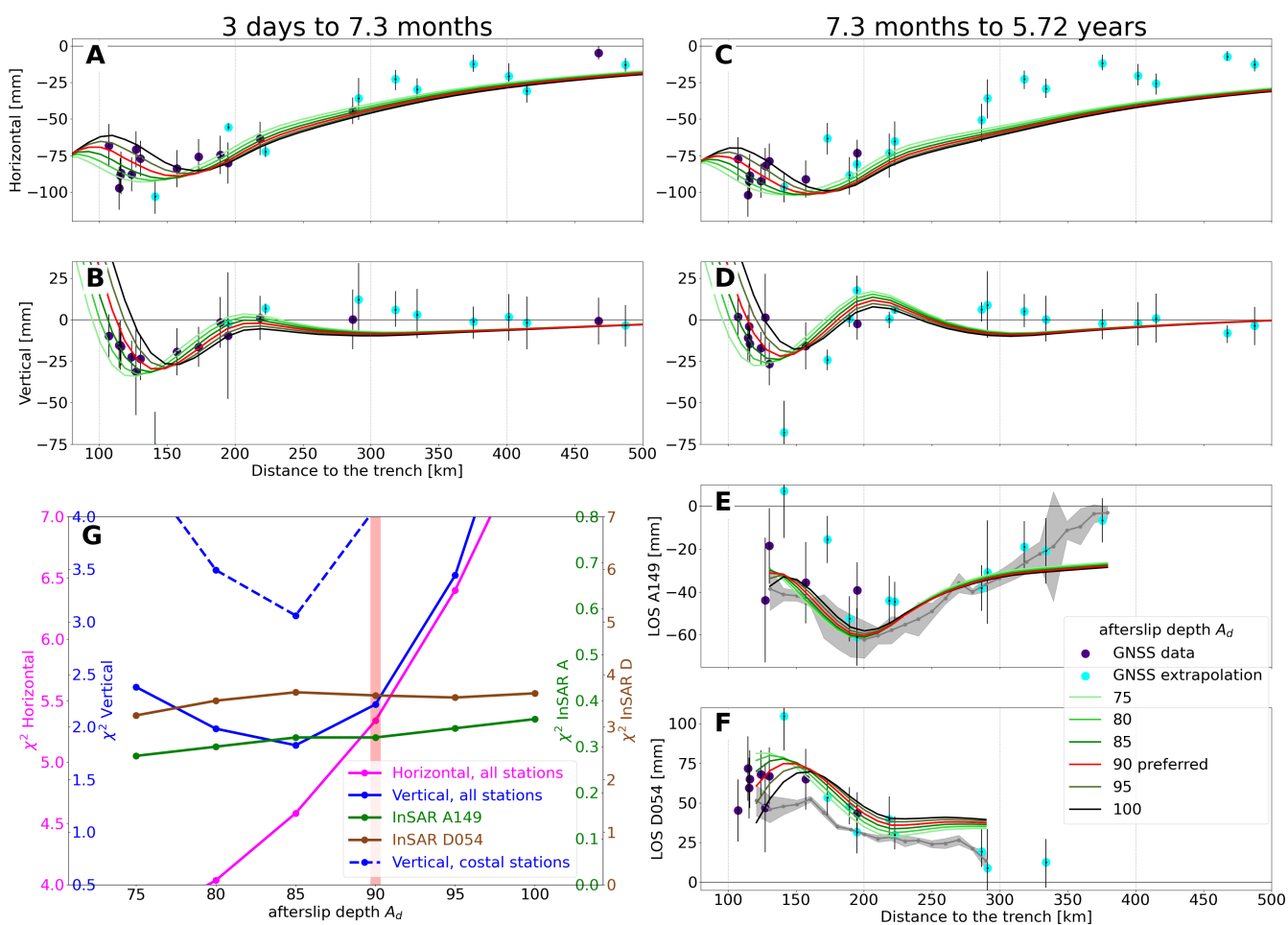


**Figure B2.** Test of the afterslip position  $A_d$ . The subfigures A, B, C, D, E and F show the same organization as in Figure 6 in the main paper. (G) shows the same organization as in Figure 7 in the main paper. Here the value of the position of the afterslip along the interface is tested. From this figure, we can conclude that an afterslip centred around 90 km from the trench fits the best the pattern observed in the data.

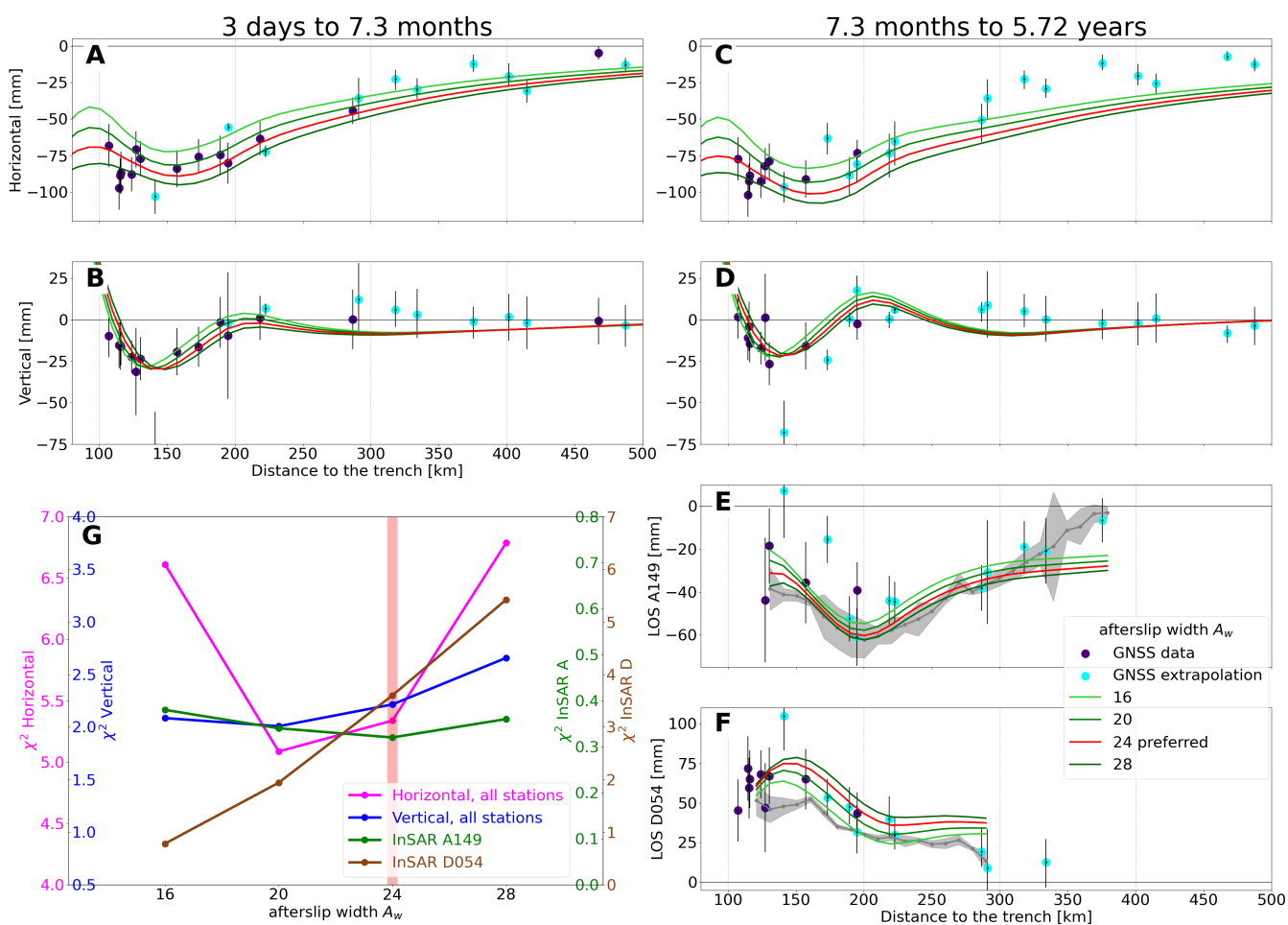


**Figure B3.** Exploration of the afterslip width  $A_w$ . The subfigures A, B, C, D, E and F show the same organization as in Figure 6 in the main paper. (G) shows the same organization as in Figure 7 in the main paper. From this figure, we can conclude that an afterslip width  $A_w = 24\text{km}$  best fits the pattern observed in the data.

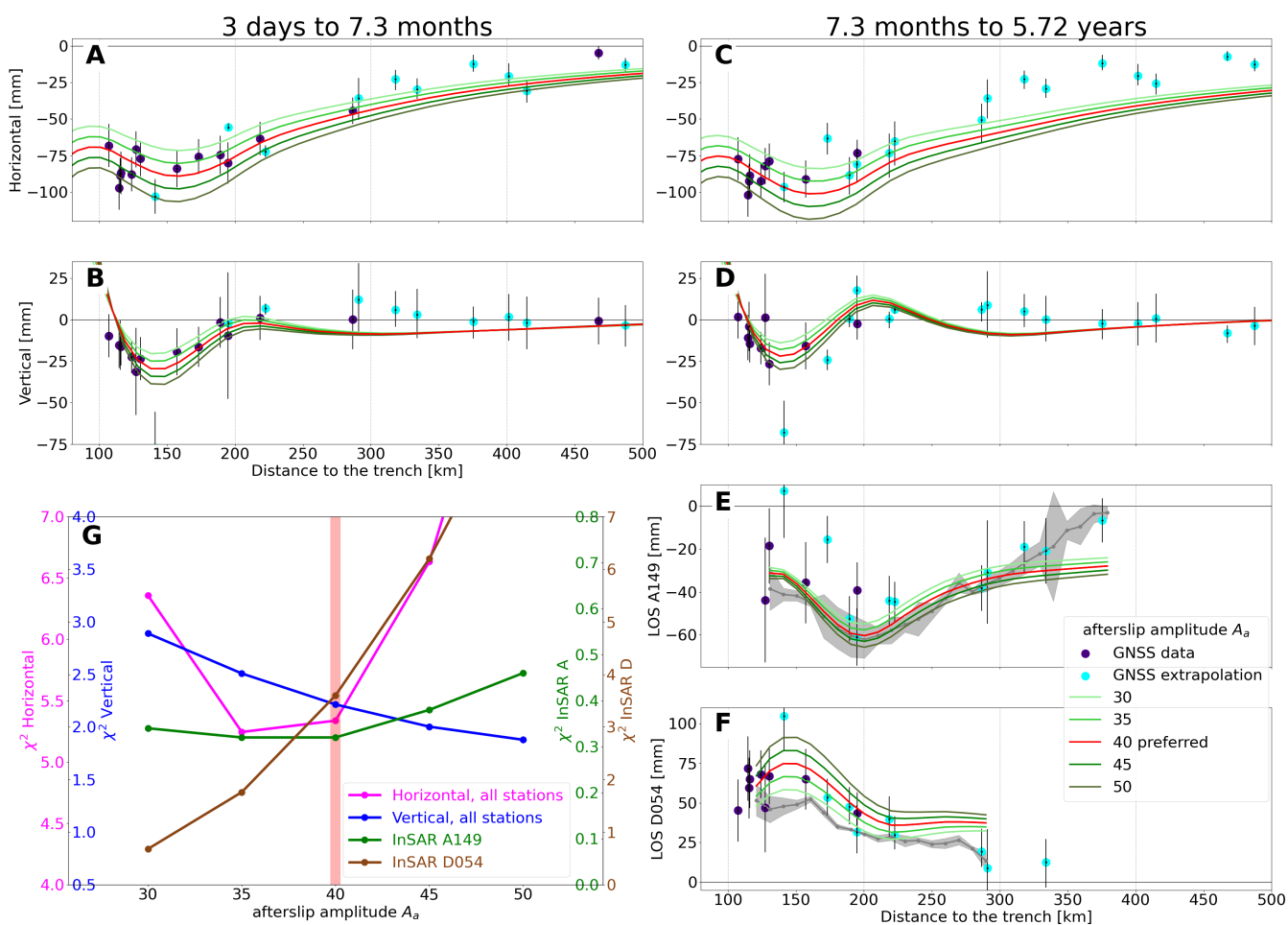


**Figure B4.** Exploration of the afterslip amplitude  $A_a$ . The subfigures A, B, C, D, E and F show the same organization as in Figure 6 in the main paper. (G) shows the same organization as in Figure 7 in the main paper. An afterslip amplitude  $A_a = 40$  cm after 6 months best fits the pattern observed in the data.